

POLYTECHNIC OF TURIN

Master's Degree  
in Nanotechnologies for ICTs



**Graphene-based Single-Molecule Junctions:  
analysis of electronic structure, transport properties  
and advantages of graphene electrodes**

Master's Degree Thesis

**Supervisors**

Prof. Mariagrazia Graziano  
Prof. Gianluca Piccinini  
M. Eng. Fabrizio Mo  
M. Eng. Chiara Elfi Spano

**Candidate**

Nicolò Guttuso

April 2023



*The Winner takes it all*

# Summary

The approaching of intrinsic limits for the scaling of silicon-based semiconductor electronic devices no longer permits to easily pursue the Moore’s law. The channel length is approaching the electron de Broglie wavelength in silicon, meaning that no control over the source to drain barrier is quantum mechanically possible for next future technological node scale lengths.

In order to meet the demand for new high-performance and low-power consumption chips, molecular electronics is one among the possible solutions, with a renewed attention gained thanks to recent advancements in terms of novel quantum mechanical transport phenomena like quantum interference. Molecular electronics aims at employing single molecules to implement electronic components: single-molecule junctions (SMJs) are the fundamental experimentally proven devices in molecular electronics, where molecules can be chosen *ad hoc* to obtain the designed features. SMJs are realized by chemically bonding molecules (usually organic molecules) between two electrodes (usually gold) via specifically chosen chemical connections or properly designed linkers. In literature there are several examples of metal and organic electrodes, including Graphene-based, but currently there are not many studies that have shown which material is the most suitable to obtain the desired conduction properties.

In this Thesis, transport properties in various graphene structures are theoretically investigated through analytic models and *ab initio* simulations following a bottom-up approach. The electronic band structure is firstly derived with a tight binding method and the analytical solution is used in the Landauer-Buttiker model for conductance in graphene sheets and nanoribbons. After a state-of-art literature overview of nanofabrication processes for graphene break junctions, such structures are then used as electrodes in SMJs to understand the advantages and drawbacks w.r.t. metal-based electrodes.

Thus, graphene-molecule-graphene single molecule junctions (GMG-SMJs) are simulated with Synopsys’ QuantumATK®, in particular OPE3, OPE5 and [3.3]pCp via amide linkages.

The obtained results show that graphene electrodes, thanks to  $\pi$ -conjugation continuity throughout the entire system, are the most natural electrodes for organic molecule-based devices, ensuring the persistence of the intrinsic properties of the molecules in contrast to metal electrodes.



# Contents

<b>1</b>	<b>Graphene properties</b>	<b>7</b>
1.1	What's graphene . . . . .	7
1.2	Electronic properties of graphene . . . . .	8
1.2.1	The honeycomb lattice of graphene . . . . .	8
1.2.2	Tight-binding method for $E(k)$ . . . . .	9
1.2.3	Density of States . . . . .	11
1.2.4	Conductance and IV relation . . . . .	13
1.2.5	Beyond monolayer pure sheet: bilayer graphene . . . . .	15
1.3	From 2D sheet to GNR . . . . .	17
1.3.1	Band Structure of aGNRs . . . . .	18
1.3.2	Density of States of aGNRs . . . . .	21
1.3.3	Conductance of aGNRs . . . . .	22
1.3.4	Simulated aGNRs . . . . .	24
<b>2</b>	<b>Productive processes</b>	<b>26</b>
2.1	Processing of graphene . . . . .	26
2.2	What's a single molecule junction . . . . .	27
2.3	Beyond gold: graphene electrodes . . . . .	30
2.4	Electroburning method . . . . .	31
2.5	Dash-line lithographic method . . . . .	32
<b>3</b>	<b>GMG-SMJ simulations</b>	<b>35</b>
3.1	QuantumATK . . . . .	35
3.2	9aGNR . . . . .	36
3.3	Benzene with 9aGNR electrodes . . . . .	37
3.4	OPE3 with 9aGNR electrodes . . . . .	40
3.5	OPE5 with 9aGNR electrodes . . . . .	43
3.6	OPE3 with graphene electrodes . . . . .	46
3.7	OPE5 with graphene electrodes . . . . .	49
3.8	OPE3 with amide linkers and graphene electrodes . . . . .	52
3.9	OPE5 with amide linkers and graphene electrodes . . . . .	55
3.10	pCp with amide linkers and graphene electrodes . . . . .	58
3.11	Conclusions and future works . . . . .	61

<b>A <math>E(\mathbf{k})</math> derivation</b>	<b>63</b>
A.1 Tight binding method . . . . .	63
A.1.1 Nearest-Neighbours approximation . . . . .	65
<b>Simulations parameters</b>	<b>69</b>
<b>Bibliography</b>	<b>72</b>

# Chapter 1

## Graphene properties

The aim of the first chapter is to give an overview of graphene, presenting an accurate analytical model for the band structure and its conductance, to be able to understand how these values change first in graphene nanoribbons and then in graphene-molecule-graphene single-molecule junctions (GMG-SMJs). After that, in the next chapters SMJs will be studied and simulated with the transport mechanisms knowledges of this chapter.

### 1.1 What's graphene

Graphene is an allotrope of carbon where ordered atoms form an honeycomb lattice in a single layer 2D structure, isolated exfoliating bulk graphite and investigated since 2004. It is formed by  $sp^2$  hybridization of Carbon, which gives it a strong mechanical resistance

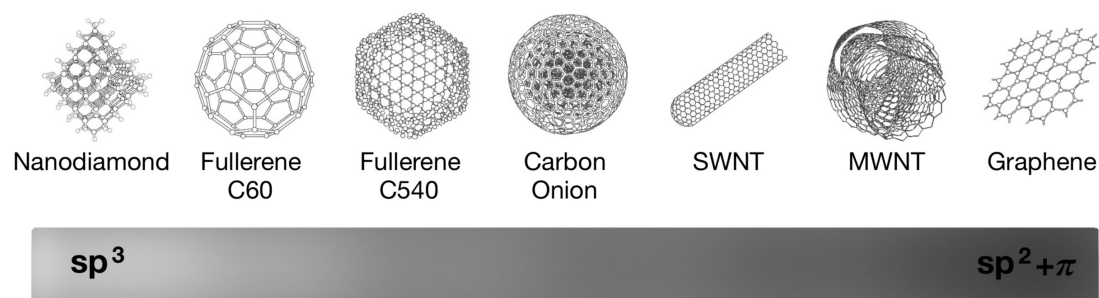


Figure 1.1. Allotropes of Carbon

due to the strong orbital planar bonding. To give an example, diamond is known to be so strong due to  $sp^3$  hybridization. The remaining  $p_z$  orbitals behave the same of aromatic compounds, creating resonant  $\pi$  bonds that favour the electron delocalization which improve the conductance: for this reason it is one of the best candidates in microelectronics, replacing more expensive and less workable metals and semiconductors<sup>[1]</sup>.

## 1.2 Electronic properties of graphene

### 1.2.1 The honeycomb lattice of graphene

First of all, since graphene is a two-dimensional material, in order to represent the entire structure it is convenient to define an  $\mathbf{R}$  vector to mathematically move within the lattice by discrete translations of the atoms as linear combination of primitive vectors

$$\mathbf{R} = n_1 \mathbf{a}_1 + n_2 \mathbf{a}_2 \quad n_1, n_2 \in \mathbb{Z} \quad (1.1)$$

having  $\mathbf{a}_1, \mathbf{a}_2$  in Cartesian coordinates where  $a_0$  is the C-C atom distance:

$$\begin{cases} \mathbf{a}_1 = \frac{a_0}{2}(\sqrt{3}, 3) \\ \mathbf{a}_2 = \frac{a_0}{2}(-\sqrt{3}, 3) \end{cases} \quad \text{with } a_0 = 1.42 \text{ \AA} \quad (1.2)$$

Consider that in this particular honeycomb lattice, figure 1.3, the defined  $\mathbf{R}$  vector allows only to move between B sites, so  $\delta_i$  vectors are needed in order to reach A ones: this particular Bravais Lattice (*bipartite lattice*) can be whole described using  $\mathbf{R}_A$  and  $\mathbf{R}_B$  vectors, where the unit cell contains two atoms.

$$\begin{cases} \delta_1 = \frac{a_0}{2}(\sqrt{3}, 1) \\ \delta_2 = \frac{a_0}{2}(-\sqrt{3}, 1) \\ \delta_3 = a_0(0, -1) \end{cases} \quad \begin{cases} \mathbf{R}_B = \mathbf{R} \\ \mathbf{R}_A = \mathbf{R} + \delta_3 \end{cases} \quad (1.3)$$

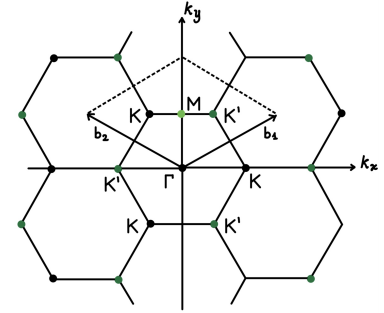
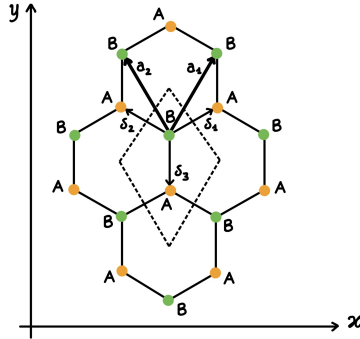
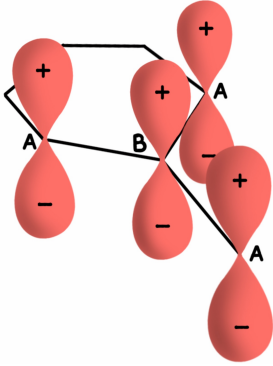


Figure 1.2.  $|2pz\rangle$  orbitals

Figure 1.3. Real lattice

Figure 1.4. Reciprocal lattice

From this geometry it is possible to define the so-called reciprocal lattice, figure 1.4, still 2D and given by all the sites where the primary cell (Brillouin Zone) is repeated:

$$\mathbf{K} = m_1 \mathbf{b}_1 + m_2 \mathbf{b}_2 \quad m_1, m_2 \in \mathbb{Z} \quad (1.4)$$

where  $e^{i\mathbf{K} \cdot \mathbf{R}} = 1$  is satisfied, meaning  $\mathbf{K} \cdot \mathbf{R} = 2\pi$  and so  $\mathbf{b}_i \cdot \mathbf{a}_j = 2\pi\delta_{ij}$ , giving as basis vectors:

$$\begin{cases} \mathbf{b}_1 = \frac{2\pi}{3a_0}(\sqrt{3}, 1) \\ \mathbf{b}_2 = \frac{2\pi}{3a_0}(-\sqrt{3}, 1) \end{cases} \quad (1.5)$$

leading to a geometry still hexagonal but rotated of  $90^\circ$ , where A and B sites are replaced by K and K'. Here Bloch's theorem imposes  $\psi_{k+K}(\mathbf{r}) = \psi_k(\mathbf{r})$ , so the reciprocal lattice can be useful to better visualize physical properties such as  $E(\mathbf{k})$  in the Brillouin zone. Here the special and useful points of the first Brillouin Zone are reported:

$$\left\{ \begin{array}{lll} \mathbf{K}_1 = \frac{2\pi}{3a_0}(\frac{2}{\sqrt{3}}, 0) & \mathbf{K}_2 = \frac{2\pi}{3a_0}(-\frac{1}{\sqrt{3}}, 1) & \mathbf{K}_3 = \frac{2\pi}{3a_0}(-\frac{1}{\sqrt{3}}, -1) \\ \mathbf{K}'_1 = \frac{2\pi}{3a_0}(-\frac{2}{\sqrt{3}}, 0) & \mathbf{K}'_2 = \frac{2\pi}{3a_0}(\frac{1}{\sqrt{3}}, -1) & \mathbf{K}'_3 = \frac{2\pi}{3a_0}(\frac{1}{\sqrt{3}}, 1) \\ \mathbf{M} = \frac{2\pi}{3a_0}(0, 1) & \mathbf{\Gamma} = (0, 0) & \end{array} \right. \quad (1.6)$$

### 1.2.2 Tight-binding method for $E(\mathbf{k})$

Since graphene has a fully periodic lattice, in order to calculate the electronic band structure it is convenient to use a tight-binding approach<sup>[2]</sup>: this method is quite useful in situations where the overlap between the atomic wave functions of different atoms is sufficiently large to require corrections from isolated atoms (atomic orbitals can no longer be the true eigenfunctions), but not so large as to render the atomic wavefunctions completely useless. The lattice Hamiltonian reads as:

$$\hat{\mathcal{H}} = -\frac{\hbar^2 \nabla^2}{2m} + U^{lat}(\mathbf{r}) \quad (1.7)$$

where the potential  $U^{lat}(\mathbf{r})$  has the periodicity of the lattice, given by the contribute of both A and B carbon atoms for each cell (mathematically speaking the same  $U_0$  potential translated by the  $\delta_3$  vector)

$$U^{lat}(\mathbf{r} + \mathbf{R}) = U^{lat}(\mathbf{r}) = \sum_{\mathbf{R}} (U_0(\mathbf{r} - \mathbf{R}) + U_0(\mathbf{r} - \mathbf{R} - \delta_3)) \quad (1.8)$$

and despite the altered potential  $U_0(\mathbf{r})$  is in theory different from the atomic isolated one  $U^{at}(\mathbf{r})$  due to the rearrangement of the electrons forming the bonds, it is convenient and fair to consider  $U_0(\mathbf{r}) \simeq U^{at}(\mathbf{r})$ .

Before solving the Schrödinger equation, since every unit cell contains two A B atoms, the lattice wavefunction has to be considered as linear combination of A and B sites

$$\psi_{\mathbf{k}}(\mathbf{r}) = f_{\mathbf{k}A}\psi_{\mathbf{k}A}(\mathbf{r}) + f_{\mathbf{k}B}\psi_{\mathbf{k}B}(\mathbf{r}) \quad (1.9)$$

where both  $\psi_{\mathbf{k}A}(\mathbf{r})$  and  $\psi_{\mathbf{k}B}(\mathbf{r})$  wavefunctions satisfy the Bloch theorem

$$\left\{ \begin{array}{ll} \psi_{\mathbf{k}A}(\mathbf{r}) = \frac{1}{\sqrt{N}} \sum_{\mathbf{R}} e^{i\mathbf{k} \cdot \mathbf{R}} \Phi_{2pz}^{at}(\mathbf{r} - \mathbf{R}_A) & \mathbf{R}_A = \mathbf{R} + \delta_3 \\ \psi_{\mathbf{k}B}(\mathbf{r}) = \frac{1}{\sqrt{N}} \sum_{\mathbf{R}} e^{i\mathbf{k} \cdot \mathbf{R}} \Phi_{2pz}^{at}(\mathbf{r} - \mathbf{R}_B) & \mathbf{R}_B = \mathbf{R} \end{array} \right. \quad (1.10)$$

having  $\Phi_{2pz}^{at}(\mathbf{r})$  the atomic wavefunction localized around the A and B carbon ion, that can be estimated from quantum chemistry. In particular, decomposing it in the Radial and Angular part, the  $|2pz\rangle$  orbital (the one important for electronic transport properties, the other shells are related to the lattice bond) has as principal, azimuthal and magnetic numbers  $n = 2, l = 1, m = 0$  respectively. As can be seen from figure 1.2 that matches the following formula, it is real and symmetric, and it is the one that favours the transport.

$$\Phi_{2pz}^{at}(\mathbf{r}) = \Phi(r, \vartheta, \varphi) = R_{n,l}(r)Y_{l,m}(\vartheta, \varphi) = R_{2,1}Y_{1,0} = R_{2,1}(r)\sqrt{\frac{3}{4\pi}}\cos\vartheta \quad (1.11)$$

Combining (1.7) and (1.9) the Schrödinger equation can be solved for the whole lattice:

$$\hat{\mathcal{H}}\psi_{\mathbf{k}}(\mathbf{r}) = E_{\mathbf{k}}\psi_{\mathbf{k}}(\mathbf{r}) \quad (1.12)$$

having as a result, in the nearest neighbours approximation, two values of the energy:

$$\varepsilon_{\mathbf{k}}^{\pm} = \frac{-\sigma_0 \pm \gamma_0|\alpha(\mathbf{k})|}{1 \mp s_0|\alpha(\mathbf{k})|} \quad (1.13)$$

where  $\sigma_0$  is constant,  $\gamma_0 \simeq 2.5 \div 3 \text{ eV}$ ,  $\alpha(\mathbf{k}) \in [0; 3]$ , and  $0 < s_0 < 0.1$ ; all calculations, details and physical interpretation of the results on appendix A.

For an initial analysis, considering the AB overlap parameter  $s_0 = 0$  the energy spectrum becomes

$$\varepsilon_{\mathbf{k}}^{\pm} = -\sigma_0 \pm \gamma_0|\alpha(\mathbf{k})| = \gamma_0\sqrt{3 + f(\mathbf{k})} \quad (1.14)$$

$$f(\mathbf{k}) = 2\cos\left(\sqrt{3}k_x a_0\right) + 4\cos\left(\frac{\sqrt{3}}{2}k_x a_0\right)\cos\left(\frac{3}{2}k_y a_0\right) \quad (1.15)$$

having the upper (+)  $\pi^*$ -band and the lower (-)  $\pi$ -band symmetric.

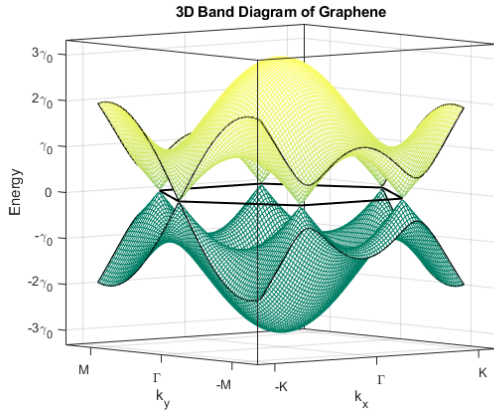


Figure 1.5. 3D  $E(\mathbf{k})$ , symmetric n-n approx

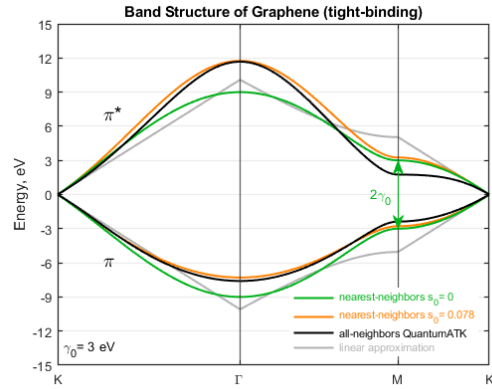


Figure 1.6.  $E(\mathbf{k})$  model comparison

Figure 1.6 shows the breaking of the symmetry when  $s_0$  is taken into account, which happens only for energies beyond  $\gamma_0$  (for example in  $\Gamma$ ). It also shows the accuracy of

nearest neighbours model when compared to all neighbours simulation with Quantum ATK<sup>T.1</sup>.

For low bias application below  $\sim 2$  V the bandstructure exhibits a symmetric behaviour and can be Taylor expanded near the  $\mathbf{K}$  and  $\mathbf{K}'$  points with the energy, for example in  $\mathbf{K}_1 = \frac{2\pi}{3a_0}(\frac{2}{\sqrt{3}}, 0)$ :

$$\varepsilon_{\mathbf{q}}^{\pm} = \pm \hbar v_F |\mathbf{q}| \quad , \quad v_F \doteq \frac{3\gamma_0 a_0}{2\hbar} \simeq 0.9 \cdot 10^6 \text{ m/s} \quad (1.16)$$

As figure 1.5 shows, equation (1.16) gives precisely the so called Dirac cones around the  $\mathbf{K}$  points, where valence and conduction bands touch in  $E = E_F$  giving a singular metallic behaviour and a linear  $E$ - $\mathbf{k}$  relation (not parabolic as in classical semiconductors): carriers travel at Fermi velocity  $v = \frac{1}{\hbar} \frac{\partial \varepsilon_{\mathbf{q}}}{\partial q}$  in the relativistic limit, behaving as relativistic massless Dirac fermions like neutrinos, having theoretical mobility values up to  $\mu \sim 100\,000 \text{ cm}^2/\text{V} \cdot \text{s}$  (best semiconductors such as GaAs reach  $\sim 9\,000 \text{ cm}^2/\text{V} \cdot \text{s}$ ). Of course the mobility is a semiconductor parameter coming from Drude model, in which electron effective mass is taken into account: however, although no mass is involved here, it is still an electrical parameter useful for estimating graphene's conductance to compare it with most common devices.

Remember that this occurs in an isolate single pure graphene sheet, without contamination, that barely happens: real estimations of  $\mu \sim 2 \div 3 \cdot 10^4 \text{ cm}^2/\text{V} \cdot \text{s}$ <sup>[3]</sup>.

### 1.2.3 Density of States

Once the Band Structure  $E(\mathbf{k})$  has been calculated, it is possible to evaluate the Density of States of graphene<sup>[4]</sup>: being a 2D structure one might expect the common staircase behaviour, but since the  $E$ - $\mathbf{k}$  relation is not parabolic things are different.

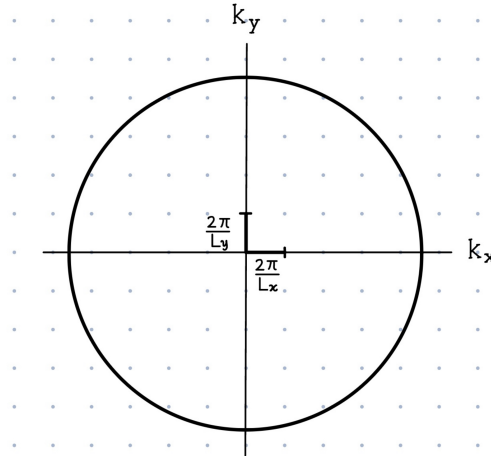


Figure 1.7.  $k$ -states in 2D space

In the reciprocal lattice the available states are spaced as shown in figure 1.7, with steps

of  $k_{x,y} = 2\pi/L_{x,y}$  due to Bloch waves conditions, so the total number of states occupied inside a circumference  $\mathbf{k}$  can be written as: (having L the lenght and W the width)

$$N_{2D} = d \frac{\pi|\mathbf{k}|^2}{\left(\frac{2\pi}{L}\right)\left(\frac{2\pi}{W}\right)} \quad (1.17)$$

where the degeneracy factor  $d = 4$  (2 for spin  $\uparrow, \downarrow$  and 2 for  $\mathbf{K}, \mathbf{K}'$  valley degeneracy). Now since the DOS can be defined as the number of states per unit of energy per unit of space:

$$\rho_{2D}(E) \doteq \frac{1}{WL} \frac{dN_{2D}}{dE} \quad (1.18)$$

to solve it linearly, around  $\varepsilon_F \pm \gamma_0$  the (1.16) approximation yields to a linear relation of DOS(E):

$$\rho_{2D}(\varepsilon) = \frac{2}{\pi(\hbar v_F)^2} \varepsilon \simeq 2 \cdot 10^{14} \frac{1}{\text{eV}^2 \text{cm}^2} \varepsilon \quad (1.19)$$

Figure 1.8 reports the estimation of the real DOS around the Fermi energy, QuantumATK<sup>T.2</sup>, where in the [-3,3] eV range it is appreciable the contribution of  $\pi$  and  $\pi^*$  Valence and Conduction bands: here, around the Dirac Cones, for energies below  $\gamma_0$ , it can be used the analytic (1.19) linear approximation, figure 1.9.

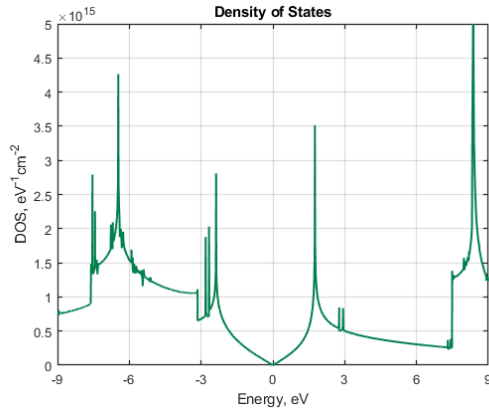


Figure 1.8. Simulated graphene sheet DOS

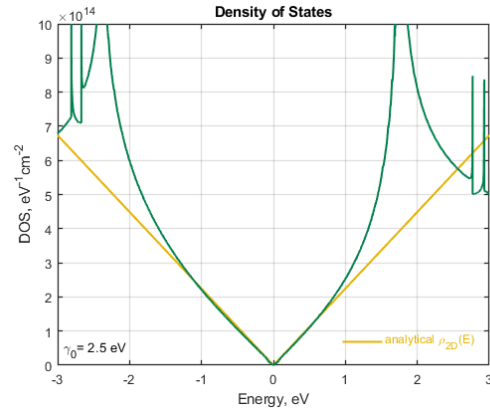


Figure 1.9. Simulated vs Analytic DOS



### 1.2.4 Conductance and IV relation

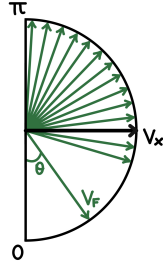
The final goal in the studying of a material is to write down the IV curve with an appropriate model. Despite graphene behaves like a metal it is not convenient to use a Drude approach since low scattering events are present, and mostly important there is no mass value since carriers are in massless relativistic limit. However, it is possible to start with the definition of current  $J = -qnv$  and treat it at the microscopic scale (so with DOS multiplied by Fermi function) in order to derive the Landauer<sup>[5]</sup> (ballistic) formula and then extend it when scattering events are present.

From the sum of all the occupied states that contribute to the current  $\mathbf{I} = -qn_L\mathbf{v}_x$ , where  $n_L$  is the carrier density per unit of length and  $\mathbf{x}$  is the direction of the flow, the total current considering the occupation probability becomes:

$$I = -q \int_{-\infty}^{+\infty} v_x \underbrace{\frac{W \rho_{2D}(|E|)}{2}}_{\text{travelling DOS}} \overbrace{(f_1 - f_2)}^{n_L(E)} dE \quad (1.20)$$

where the under brace DOS is a density per unit of energy per unit of length and it is divided by 2 because half of the states travel from left to right (source (1) to drain (2)) weighted by Fermi function  $f_1$ , and the other half from right to left. The total current will be the difference of the two fluxes, explained by the  $(f_1 - f_2)$  factor.

The last consideration needed is about the unknown velocity component  $v_x$  of the carriers: in principle  $v$  can assume all the angles from 0 to  $\pi$  that belong to the semicircle facing the transport direction, so it has to taken into account the average in the x direction.



$$v_x = \frac{1}{\pi} \int_0^\pi v_F \sin(\vartheta) d\vartheta = \frac{2}{\pi} v_F \quad (1.21)$$

In the case of graphene  $\rho_{2D}$  has been calculated one at (1.19), substituting it and (1.21) into (1.20) the final Landauer formula reads as:

$$I = -\frac{2q}{h} \int_{-\infty}^{+\infty} M(E) (f_1 - f_2) dE \quad (1.22)$$

$$\text{with } M(E) = \frac{2W}{\pi \hbar v_F} |E|, \quad f_j(E, T) = \frac{1}{e^{\frac{E - \mu_j}{k_B T}} + 1} \quad (1.23)$$

where  $M(E)$  represents the number of modes that contributes to transport<sup>[6]</sup>.

This equation is valid in the ballistic limit, where electrons travel from source to drain without any scattering. To take into account scattering events, a generalization of this formula,

the Landauer-Büttiker formalism, considers a Transmission probability  $0 \leq T(E) \leq 1$  proportional to the mean free path of the carriers (the travelled space before a scattering event occurs):

$$T(E) = \frac{\lambda(E, T)}{\lambda(E, T) + L} \quad \left\{ \begin{array}{l} \text{Diffusive:} \\ L \gg \lambda \\ T = \frac{\lambda}{L} \ll 1 \\ \\ \text{Ballistic:} \\ L \ll \lambda \\ T \rightarrow 1 \\ \\ \text{Quasi-ballistic:} \\ L \approx \lambda \\ T < 1 \end{array} \right. \quad (1.24)$$

where (1.22) becomes weighted by the probability of carriers to contribute to the total current:

$$I = -\frac{2q}{h} \int_{-\infty}^{+\infty} \underbrace{T(E)}_{\text{Transmission}} \underbrace{M(E)}_{\text{Spectrum}} (f_1 - f_2) dE \quad (1.25)$$

In other words, the evaluated current can be seen as the area integrated in the Bias Window - by the external applied voltage  $\Delta V$  - below the so called Transmission Spectrum: for example, with a bias of 2 V, the current will be given by the area in the range  $[-1, 1]$  eV below the black curve (TS) on figure 1.10.

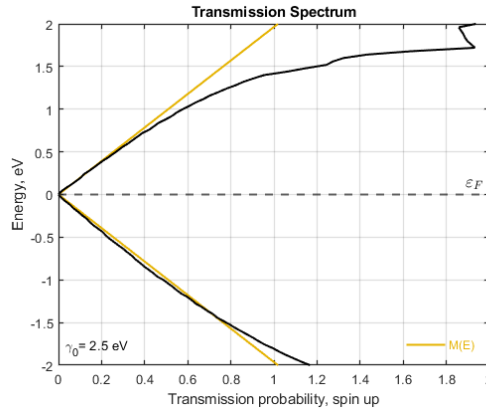


Figure 1.10. TS for graphene primitive cell

It is important to make some considerations about  $\lambda(E, Temp)$ : in graphene the evaluation of the mean free path is still an active field of research, where the goal is to correctly estimate each scattering contribution, such as acoustic phonon scattering ( $\propto Temp$ ), charged impurity scattering ( $\propto E$ ) or defects scattering.

With QuantumATK it is possible to estimate  $\lambda$ : since it calculates TS, knowing the analytical travelling mode function  $M(E)$ , one can calculate the Transmission Probability  $T(E)$ .

In the 1.10 graph TS has been calculated for the primitive cell (figure 1.3) of graphene<sup>T.3</sup>: with a width  $W = 3a_0$  the travelling modes follow  $M(E) = \frac{4|E|}{\pi\gamma_0}$ , yellow curve, where they almost overlap TS, suggesting a probability  $T=1$ . In this case the conduction is in fact ballistic, since  $L$  of the primitive cell is much lower than  $\lambda$ , estimated to be around  $\sim 300$  nm at room Temperature. Notice that for whatever other primary cell it would change  $W$  and so  $M$  and proportionally TS, but having  $T$  always equal to 1. For example doubling the cell in the transversal direction, so doubling  $W$ ,  $M$  and TS will double. For seeing a change in  $T$   $L$  should be longer than  $\sim 500$  primary cells. These results are in perfect agreement with the conductance expectations: since  $T \propto 1/L$  and  $M \propto W$ , for a graphene sheet geometry behaves as in macrophysics  $G \propto T(E)M(E) \propto W/L$ .

Also from the Landauer-Büttiker formula (1.25) it is possible to explicitly write the conductance, where for low external bias the Fermi statistics can be Taylor expanded to  $f_1 - f_2 = -\partial_E f_0(\mu_2 - \mu_1)$ , with  $(\mu_2 - \mu_1) = -q\Delta V$ :

$$G = \frac{I}{\Delta V} = \frac{2q^2}{h} \int_{-\infty}^{+\infty} T(E) M(E) \left( -\frac{\partial f_0}{\partial E} \right) dE \quad (1.26)$$

### 1.2.5 Beyond monolayer pure sheet: bilayer graphene

In real applications the graphene sheet is neither infinite nor pure, leading to scattering events (impurity) that lower  $\lambda$  and so mobility  $\mu$ .

Also in real devices, the monolayer sheet is often unstable and tends to fold itself, so it is more probable to see multilayer graphene sheets to achieve more stability, which exhibit intermediate properties between graphene and graphite. It is important to analyse how Energy, Dos and Conduction change when going beyond the single pure sheet: the simplest case is the bilayer one, that can be constructed with different stacking methods.

Here it is analysed the most energetically favoured, the A-B one (Bernal stacking), where the A sites of the top layer are placed exactly above the B sites of the bottom layer, figure 1.11 : replicating this stacking method graphite is obtained.

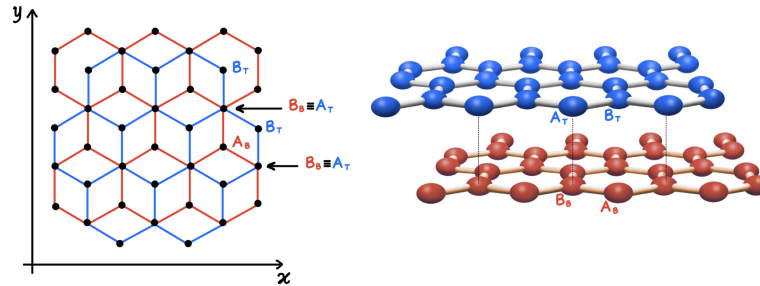


Figure 1.11. A-B Bernal Stacking for bilayer graphene

Having 4 atoms for primary cell, the solution of Schrödinger equation will give a band structure with 4 bands, figure 1.12, with energy<sup>[7]</sup>:

$$\varepsilon_{\mathbf{k}} = \pm \frac{\gamma_{\perp}}{2} \pm \sqrt{\frac{\gamma_{\perp}^2}{4} + \gamma_0^2 |\alpha(\mathbf{k})|^2} \quad (1.27)$$

Where around  $\mathbf{K}$  and  $\mathbf{K}'$  points the bands lose the metallic Dirac Cones, exhibiting a semiconductor behaviour (indeed graphite has a parabolic band diagram) with increased effective mass and so mobility drastically reduced, changing the conductance:

$$\varepsilon_{\mathbf{q}}^{\pm} = \pm \frac{\hbar^2 \mathbf{q}^2}{2m^*} \quad , \quad m^* = \frac{|\gamma_{\perp}|}{2v_F^2} \simeq 0.054m \quad , \quad \gamma_{\perp} \simeq 0.4 \text{ eV} \quad (1.28)$$

with  $\gamma_{\perp}$  due to the coupling of  $|2pz\rangle$  orbitals between  $A_t - B_b$  touching sites.

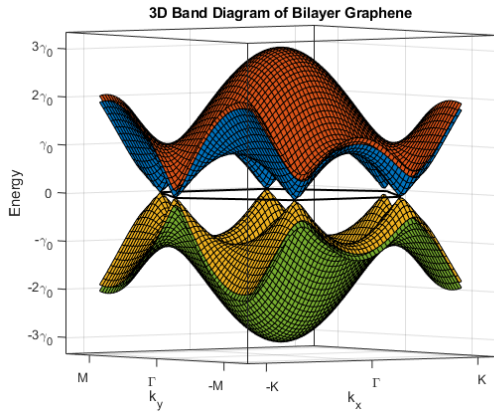


Figure 1.12. 3D  $E(\mathbf{k})$   $A_t - B_b$  bilayer graphene

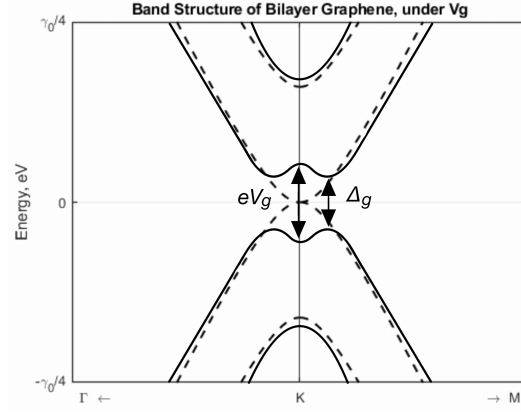


Figure 1.13.  $E(\mathbf{k})$  tunable gap under  $V_g$

A peculiarity of this bilayer is that under perpendicular “gate”  $V_g$  voltage it exhibits a tunable gap: in particular, in the low bias regime  $\hbar v_F |\mathbf{q}| \ll eV_g \ll \gamma_{\perp}$ , equation (1.27) around  $\mathbf{K}$  becomes

$$\varepsilon_{\mathbf{q}} \simeq \pm \left( \frac{eV_g}{2} - \frac{eV_g \hbar^2 v_F^2}{2\gamma_{\perp}^2} |\mathbf{q}|^2 + \frac{\hbar^4 v_F^4}{\gamma_{\perp}^2 eV_g} |\mathbf{q}|^4 \right) \quad (1.29)$$

that gives a gap in  $\mathbf{K}$  equal to  $eV_g$ , figure 1.13, and creates tunable indirect bandgaps in  $\mathbf{q} = \pm |eV_g| / (2\hbar v_F)$  equal to:

$$\Delta_g = |eV_g| \left( 1 - \frac{(eV_g)^2}{\gamma_{\perp}^2} \right) \quad (1.30)$$

This tunable gap is quite promising for potential application in optoelectronic devices, but it can also be a drawback in graphene electrodes, where uncontrolled  $V_g$  leakage (gate screening) could change  $E(\mathbf{k})$  and so unpredictably the conduction.

The take home message is that going beyond pure monolayer sheet properties change, as in GNRs of following section.

### 1.3 From 2D sheet to GNR

In real device applications with nanometric sizes, graphene sheets are cut and shaped, where the dangling bonds of the edges are usually saturated with hydrogen: in this case, for stripes below 100 nm, the so called graphene nanoribbons (GNRs) are created. Based on the orientation of the cut the GNRs will exhibit different physical and transport properties<sup>[8]</sup>: the most common cuts are those with *zigzag* edges and *armchair* edges, rotated 30 degrees with respect to one another, figure 1.14.

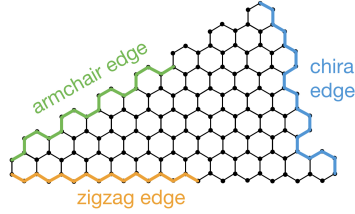


Figure 1.14. Edge cuts for graphene nanoribbons

Being structures with a width below 100 nm ( $\sim$  thousands of atoms), GNRs exhibit quantum confinement on the lateral dimension with respect to the transport direction: the thickness of the ribbon greatly influences the transport properties, the thinner the structure the more confined it is, the wider it is and the more it tends to bulk.

Since in simulated graphene-molecule-graphene junctions the electrodes reach even a single atom thickness at the tip of the gap, it is therefore fundamental to analyze how the 2D DOS and conductance properties of graphene sheets change in 1D confined structures. Therefore, since width is a fundamental parameter for classifying GNRs, it is useful to have a thickness-number of width atoms relation  $W(N)$ , with  $N$  according to figures 1.15 and 1.16:

$$\begin{cases} W_a = \frac{\sqrt{3}}{2}(N-1)a_0 & \text{for armchair ribbons} \\ W_z = \frac{6N-7-(-1)^N}{8}a_0 & \text{for zigzag ribbons} \end{cases} \quad (1.31)$$

the lengths of the C-H bonds of the first and last atom should be added to the widths.

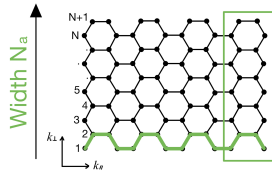


Figure 1.15. Armchair N counting

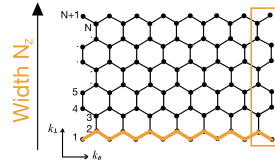


Figure 1.16. Zigzag N counting

### 1.3.1 Band Structure of aGNRs

Since in the simulated junctions electrodes with armchair orientation will be used, it is necessary to study how their band structure changes with respect to the Dirac cones of the pristine sheet.

To obtain the energy dispersion relation, confinement along the Width  $W$  has to be applied in the Hamiltonian of the aGNRs, imposing Dirichlet Boundary Conditions and so zero wavefunction in the first and last atoms of the chain<sup>[9]</sup>. In a GNR with  $N$  atoms of carbon, considering C-H bonds also:

$$\Psi(0) = \Psi(N+1) = 0 \longrightarrow Ae^{ik_{\perp}W} = 0 \longrightarrow k_{\perp}W = p\pi \quad (1.32)$$

meaning confined stationary waves along the perpendicular direction to the transport.

To see the quantization of the wave vector  $k_{\perp}$ , having  $p$  an integer,  $W_a$  of (1.31) can be substituted, approximating C-H bond length as C-C:

$$k_{\perp} = \frac{2}{\sqrt{3}a_0} \frac{p\pi}{N+1} \quad , \quad p = 1, \dots, N \quad (1.33)$$

Now the new Hamiltonian  $\hat{\mathcal{H}}\Psi_{\mathbf{k}}(\mathbf{r}) = E_{\mathbf{k}}\Psi_{\mathbf{k}}(\mathbf{r})$  can be solved as done in graphene sheet: (Notice that the following formula<sup>[10]</sup> is centered in  $\mathbf{k} = \mathbf{K}$  and no more in  $\mathbf{k} = \mathbf{\Gamma}$ )

$$E_{\mathbf{k}} = \pm\gamma_0 \sqrt{1 + 4 \cos\left(\frac{p\pi}{N+1}\right) \cos\left(\frac{3}{2}a_0\mathbf{k}\right) + 4 \cos^2\left(\frac{p\pi}{N+1}\right)} \quad (1.34)$$

where the integer  $p$  from 1 to  $N$  indicates the  $p$ -subband of the dispersion relation, meaning more subbands for larger ribbons.

Notice also that these subbands are not ordered from low to high energies, the first  $E_c$  and  $E_v$  bands assume values of  $p$  different from 1.

Looking at  $\mathbf{k} = 0$ , where in the sheet was the Dirac cone, here the band structure becomes:

$$E_{\mathbf{k}} = \pm\gamma_0 \left(1 + 2 \cos\left(\frac{p\pi}{N+1}\right)\right) \quad (1.35)$$

in which unlike the Dirac cone it goes to zero only if:

$$E_{\mathbf{k}} = \pm\gamma_0 \left(1 + 2 \cos\left(\frac{p\pi}{N+1}\right)\right) = 0 \implies 2(N+1) = 3p \quad (1.36)$$

and since  $p$  and  $N$  are integers, the latter condition is verified only for certain  $N$ .

Writing the carbon atoms number as  $N = 3m - 1$  (with  $m$  integer),  $p$  must be  $p = 2m$ . It means that for all aGNRs having  $N = 3m - 1$  ( $N=2,5,8,11,14..$ ) first  $E_c$  and  $E_v$  bands (corresponding to the index  $p = 2m$ ) touch each other in  $E = 0$ , so with an energy gap  $\Delta_a = 0$ , having a metallic behaviour<sup>[11]</sup>.

For all other values of  $N$  the (1.36) condition is not satisfied, ribbons will have  $E(\mathbf{K}) \neq 0$  and so direct band gaps.

Plotting (1.34) it can be easily shown that for others  $N$  (in general, keeping the notation with  $m$ , the ones with  $N = 3m$  and  $N = 3m + 1$ ) first  $E_c$  and  $E_v$  bands will be the subbands with  $p = 2m + 1$  index.

So knowing the correspondent  $p$  index, the gaps can be estimated for all types of aGNR:

$$\Delta_a = \begin{cases} 0 & N = 3m - 1 \\ 2\gamma_0 \left| 1 + 2 \cos\left(\frac{2m+1}{3m+1}\pi\right) \right| & N = 3m \\ 2\gamma_0 \left| 1 + 2 \cos\left(\frac{2m+1}{3m+2}\pi\right) \right| & N = 3m + 1 \end{cases} \quad m = 1, \dots, M \quad (1.37)$$

where  $\Delta_a^{3m} \gtrsim \Delta_a^{3m+1} > \Delta_a^{3m-1} = 0$ , for each  $m$ .

Plotting (1.37), figure 1.17, it can be seen how increasing  $N$  (and so  $W$ ), gaps decrease with  $\propto 1/W$ , exactly as expected since they tend to zero gap of pristine sheets.

The gap in the energy dispersion relation plays a fundamental role in the conduction of graphene electrodes junctions, since no bands at low energies means no available states and so null transmission probability.

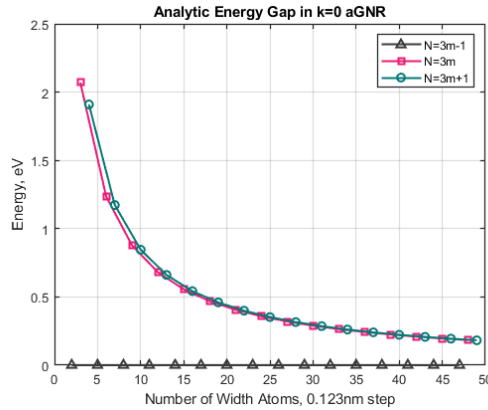


Figure 1.17. Pristine aGNRs, no edge effects

No e-e interaction or Spin and Temperature dependencies have been considered since the aim is to reveal the intrinsic difference in the p electronic state originating from the topological nature of the various ribbon edges, without edge effects.

Considering edge effects<sup>[12]</sup>, meaning perturbations due to Hydrogen in C-H bonds (as QuantumATK does), real gaps are slightly different, actually having  $\Delta_a^{3m+1} > \Delta_a^{3m} > \Delta_a^{3m-1} \neq 0$  meaning higher  $3m + 1$  and nonzero  $3m - 1$ , while lower  $3m$ .

Once gaps has been estimated, knowing first p-subbands the dispersion relations (1.34) can be Taylor expanded in  $\mathbf{k} = 0$  ( $\mathbf{K}$  point) to know band structures for low bias applications:

$$E_{\mathbf{k}} \approx \begin{cases} \frac{3}{2}a_0\gamma_0|\mathbf{k}| & N = 3m - 1, \quad p = 2m \\ \frac{\Delta_a}{2} - \frac{\gamma_0^2}{\Delta_a} 2 \cos\left(\frac{2m+1}{3m+1}\pi\right) \left(\frac{3}{2}a_0\mathbf{k}\right)^2 & N = 3m, \quad p = 2m + 1 \\ \frac{\Delta_a}{2} - \frac{\gamma_0^2}{\Delta_a} 2 \cos\left(\frac{2m+1}{3m+2}\pi\right) \left(\frac{3}{2}a_0\mathbf{k}\right)^2 & N = 3m + 1, \quad p = 2m + 1 \end{cases} \quad (1.38)$$

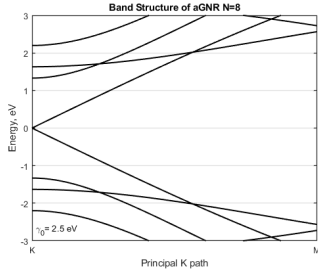


Figure 1.18. aGNR N=8

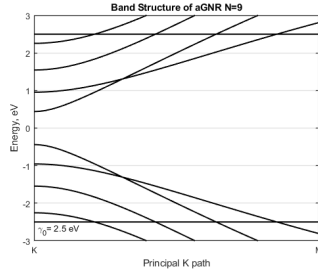


Figure 1.19. aGNR N=9

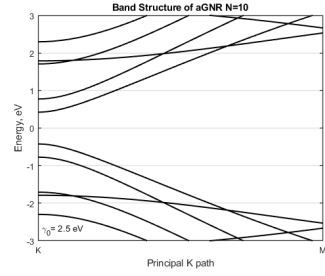


Figure 1.20. aGNR N=10

with the respective  $\Delta_a(N)$ . Since  $N = 3m - 1$  ones (fig. 1.18) have zero gap and linear  $E(\mathbf{k})$ , same slope as Dirac cones, are called metallic aGNRs. Instead  $N = 3m$  (fig. 1.19) and  $N = 3m + 1$  (fig. 1.20) with gaps and parabolic behaviour are semiconductive aGNRs. Increasing  $W$ , as fig. 1.21,  $E(\mathbf{k})$  tends to the sheet one, figure 1.6 (from  $\mathbf{K}$  to  $\mathbf{M}$  point).

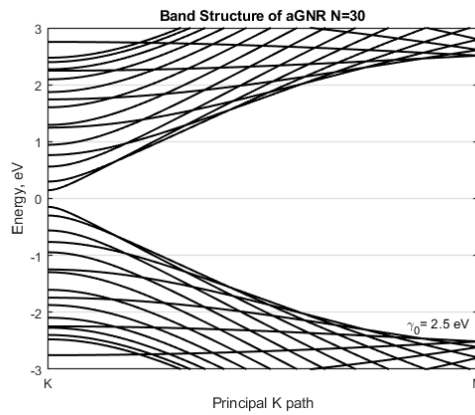


Figure 1.21. aGNR N=30



### 1.3.2 Density of States of aGNRs

Switching from 2D system of the sheet to 1D system also changes the density of states, that follows the typical  $\propto 1/\sqrt{E}$  for each parabolic band of classical semiconductive wires.

In particular, following the definition of DOS similarly to equations (1.17) and (1.18) for 1D case, with the number of  $\mathbf{k}$  states spaced by Bloch conditions:

$$\rho_{1D}(E) \doteq \frac{1}{L} \frac{dN_{1D}}{dE} \quad \text{with} \quad N_{1D} = d \frac{2|\mathbf{k}|}{\left(\frac{2\pi}{L}\right)} \quad (1.39)$$

To solve  $\rho_{1D}(E)$  it has to be used the full  $E(\mathbf{k})$  (1.34) relation.

To linearize and see analytically the value of the DOS, in the semiconductive case, the parabolic bands can be written as subbands with a certain efficacy mass  $m^*$ : the DOS will be zero along the gap and then the sum of all  $1/\sqrt{E}$  peaks for each subbands, figure 1.22.

$$E_{\mathbf{k}} = \frac{\hbar^2 \mathbf{k}^2}{2m^*} \quad \Rightarrow \quad \rho_{1D}(E) = \frac{d\sqrt{2m^*}}{h\sqrt{E}} \quad (1.40)$$

In the metallic case, in which the first  $E_c$  and  $E_v$  subbands are linear with no gap, the solution of the DOS will be a step function starting from  $E = 0$ .

For second and successive bands, having parabolic behaviours, same as semiconductor happens, figure 1.23:

$$E_{\mathbf{k}} = \hbar v_F \mathbf{k} \quad \Rightarrow \quad \rho_{1D}(E) = \frac{d}{\pi \hbar v_F} \quad (1.41)$$

Note that in classic operating ranges, low bias, only the first 2-3 subbands are involved.

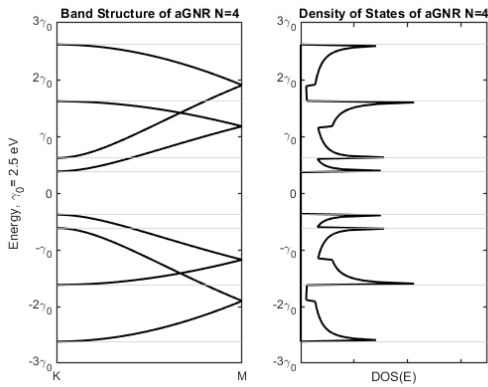


Figure 1.22. DOS for sem-aGNR N=4

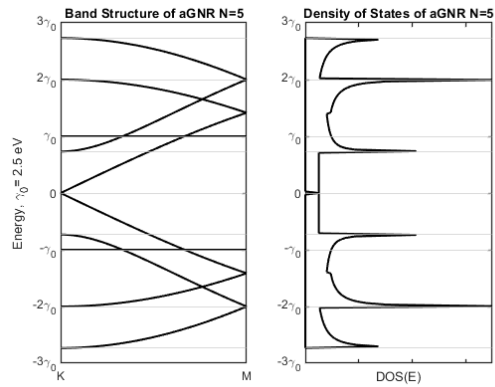


Figure 1.23. DOS for met-aGNR N=5

Of course for larger ribbons, increasing  $N$  there will be more  $p$  (up to  $N$ ) subbands, meaning more contributes from all peaks in DOS: also here as for the band structure the DOS of figure 1.24 tends to bulk of figure 1.9.

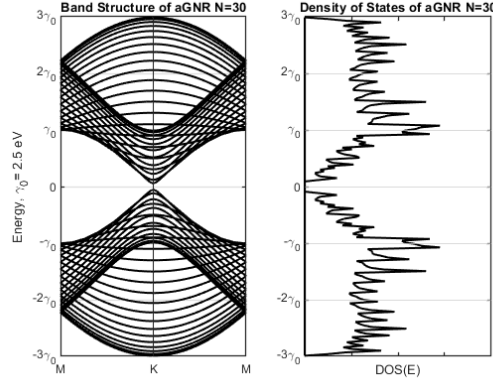


Figure 1.24. DOS for aGNR  $N=30$

In real wires, where hydrogen perturbations occur at edges<sup>[13][14]</sup>, having slightly wider gaps, the first available states will start at slightly higher energies (except for  $3m$ , having as explained before lower gaps).

### 1.3.3 Conductance of aGNRs

Once a model for the states for all possible ribbons has been computed, a current model proportional to carrier density can be done, where the 1D analogous of (1.20) becomes exactly the Landauer model in a nanowire:

$$I = -q \int_{-\infty}^{+\infty} v(E) \frac{\rho_{1D}(|E|)}{2} (f_1 - f_2) dE \quad (1.42)$$

Despite analytical  $\rho_{1D}$  has not been solved, the current can be rewritten just considering the (1.39) definition with the degeneracy factor  $d = 2$  for double Spin  $\uparrow\downarrow$ , and with the velocity contribution of each subband (both for metallic and semiconductive cases) given by  $v(E) = \frac{1}{\hbar} \frac{dE}{dk}$ :

$$I = -\frac{2q}{h} \int_{-\infty}^{+\infty} (f_1 - f_2) dE \quad (1.43)$$

Where basically the (1.22) Landauer gets quantized travelling modes  $M(E)=1$  for each subband, so with a more general  $M(E)=n$  with  $n$  the number of subbands that contribute to electronic transport, valid for all bands and all ribbons<sup>[15]</sup>.

The conductance, if ballistic regime and so  $T(E)=1$  is considered (reliable for typical electrodes lengths), reads as (for each band):

$$G = \frac{I}{\Delta V} = \frac{2q^2}{h} \int_{-\infty}^{+\infty} \left( -\frac{\partial f_0}{\partial E} \right) dE \quad (1.44)$$

In the limit of perfect edges at zero temperature, the quantized (1.44) conductance can be simplified as:

$$G = \frac{2q^2}{h} g(E) \quad (1.45)$$

In which  $g(E)=n(E,W)$ .

Figure 1.25 shows the contribution of each subbands to the quantized conductance.

As expected from macrophysics, where the section of wires is proportional to electrical conductivity, also here for wider ribbons with more subbands  $g(E)$  increases: with same external  $V_{ds}$  applied, higher  $N(W)$  means more atoms, so orbitals and conductive states: more modes contribute to transport, figure 1.26.

This figure also shows how the whole  $E(k)$ ,  $DOS(E)$  and  $G(E)$  models of NanoRibbons reach the graphene ones if ribbons gets larger: yellow curve is the travelling mode relation of (1.23), with the proper width  $W_a$  calculated from (1.31) definition,  $M(E) = \frac{2(N+1)}{\sqrt{3}\pi\gamma_0} E$ , that fits a completely different model of  $g(E)$ .

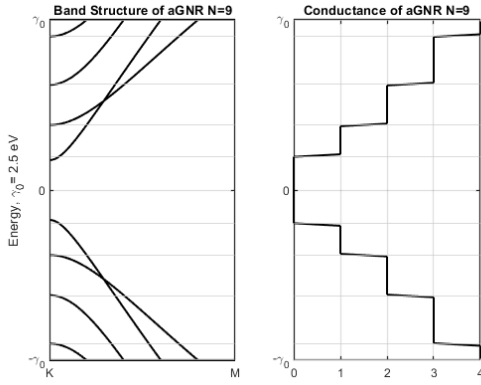


Figure 1.25.  $g(E)$  for aGNR  $N=9$

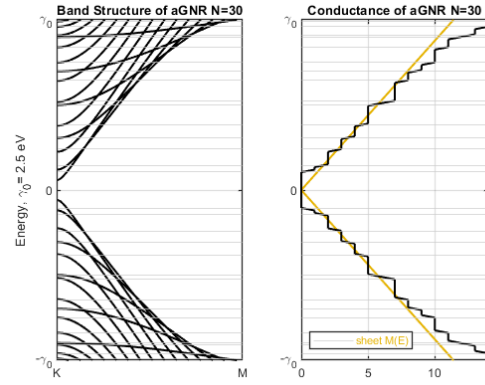


Figure 1.26.  $g(E)$  for aGNR  $N=30$

If a Landauer-Buttiker model would be considered, the conductance can be corrected with a transmission probability factor that takes into account diffusive limits and real disorders:

$$G = G_0 g(E) \tilde{t}(E) \quad (1.46)$$

in fact, depending on the distribution of the defects, a diffusive transport regime or even Coulomb blockade effects may occur instead of ballistic conductance.

Note that subbands in the dispersion relation have finite limits, meaning that  $g(E)$  is not strictly a monotonically non-decreasing function: the wire can have a negative differential resistance, in particular for energies above  $\gamma_0$  (check 1.24 DOS graph).

No electron-electron interaction and spin polarization effects have been considered with the Landauer formula, being a reduced model of the more general Meir–Wingreen formula for mesoscopic system<sup>[16]</sup>.

### 1.3.4 Simulated aGNRs

To validate these Band Structure, Density of States and Conductance models a short 9aGNR wire and a long 30aGNR one have been simulated with QuantumATK<sup>T.4</sup>.

#### Example case aGNR N=9

The following graphs for a 9aGNR show how they match the predictions of figure 1.25, having a slightly lower gap due to edge effects coming from hydrogen perturbations of C-H bonds, in particular getting "real"  $E_g = 0.70$  eV compared to analytic  $\Delta_a = 0.88$  eV. The other main difference is the asymmetry of Conductance and Valence bands, considered by the  $s_0$  overlap parameter in the complete analytical tight binding method for  $E(\mathbf{k})$  in the graphene sheet but not in the simplified band structure of the ribbons of equation (1.34): real structures present more  $\pi^*$  conductive bands and so steps in the conductance. Since the Transmission Spectrum given by QuantumATK is equal to the  $G = G_0 g(E)$  conductance, the transmission probability is  $\tilde{t}(E) = 1$ , meaning ballistic regime.

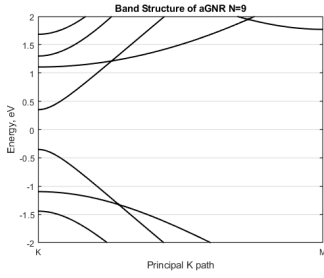


Figure 1.27. BS 9aGNR

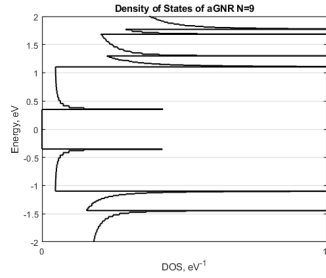


Figure 1.28. DOS 9aGNR

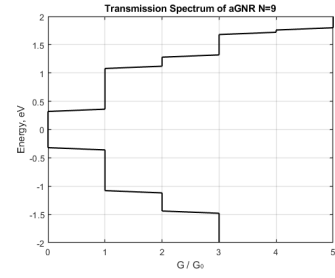


Figure 1.29. TS 9aGNR

#### Example case aGNR N=30

With the long 30aGNR same happens: "real" gap  $E_g = 0.24$  eV is slightly lower than the analytic  $\Delta_a = 0.29$  eV. The high number of bands highlights the asymmetry of the states: TS starts to become similar to the simulated sheets one, 1.10, also having NDR.

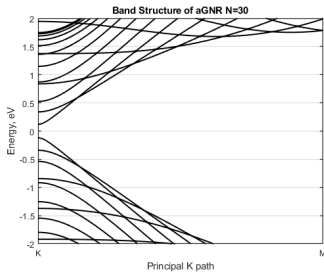


Figure 1.30. BS 30aGNR

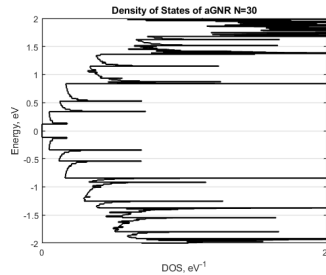


Figure 1.31. DOS 30aGNR

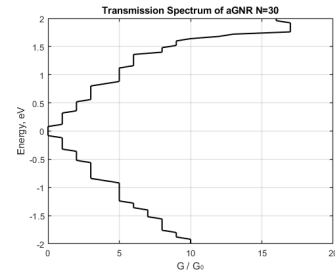


Figure 1.32. TS 30aGNR



## Chapter 2

# Productive processes

After have shown an accurate analytical model for conduction in graphene, it is fundamental to know how it is manufactured in industrial processes, to be able to understand how sheets are firstly created and then cut to create graphene-based molecular junctions: knowing how real devices are made, it is possible to accurately simulate them to predict their electronic transport and physical properties.

The focus of these chapter will be based on the technological steps needed to create real graphene-molecule-graphene single molecule junctions (GMG-SMJs), and their basic working principles.

### 2.1 Processing of graphene

The realization of graphene-based molecular junctions relies on high-yield and low-cost synthesis methods of graphene layers, subsequently developed into break-junctions.

Most involved techniques for processing carbon derive from deposition processes, as plasma-enhanced chemical vapor deposition<sup>[17]</sup> (PE-CVD), where the plasma rich chemical environment allows lower temperature operating ranges and faster growth than classical CVDS. Carbon gases such as  $\text{CH}_4$  with  $\text{H}_2$  mixtures are injected in chambers at growth temperatures spacing from  $400^\circ\text{C}$  to  $700^\circ\text{C}$ , usually on Ni or Cu foils coated on  $\text{SiO}_2$  substrate, that guarantee high quality single layer graphene (SLG) formation thanks to low carbon solubility and catalytic nature of metals.

Subsequent processing of graphene can lead to the production of carbon nanotubes (CNTs) or different fullerenes, widely engineered in opto and micro electronics, biomedical applications, energy management and chemical treatments<sup>[18]</sup>.

In the case of GNRs different growth methods are exploited<sup>[19]</sup>: the best ones are from epitaxial growth on polished  $\text{SiC}(0001)$  in ultra high vacuum (UHV), to achieve high quality atomic resolution control. Also bottom-up approaches are studied, both solution-mediated synthesis with  $sp^2$  organic mixtures, and surface-assisted synthesis on  $\text{Au}(111)$ . Once graphene single or multi layers are obtained, they can be treated in molecular electronics, first in the fabrication of graphene break-junctions and subsequently into graphene-based single molecule junctions.

## 2.2 What's a single molecule junction

In order to overcome the limitations of scaling processes of silicon-based devices, several alternatives have been proposed in the past decades, updated every year by the International Technology Roadmap for Semiconductors (ITRS). Molecular electronics is one of these, where the idea is to develop nanosystems in which the conductivity of single molecules can be modulated by electrical, optical, thermal (chemical, mechanical, ...) stimuli, creating optimally engineered ultrasmall sized devices such as transistors, sensors, switches and so on<sup>[20][21]</sup>.

Several techniques are possible for constructing single-molecule-junctions, where the general approach is to bond a designed (usually organic) molecule between two fabricated electrodes, via specifically chosen chemical connections or properly designed linkers.

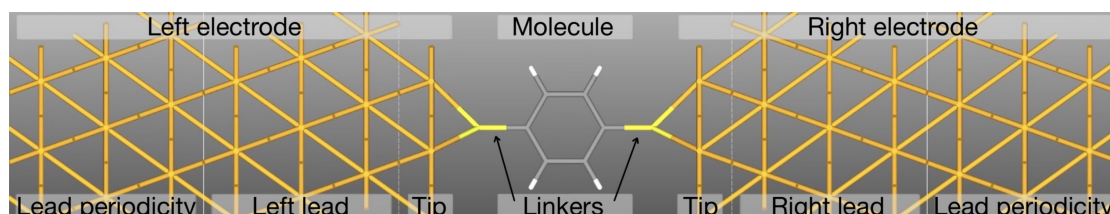


Figure 2.1. Example of Benzene molecule wire with gold electrodes and thiol linkers

### Molecule

The electronic transport is characterized by the organic molecule quantized HOMO-LUMO levels, that substitute the Conduction and Valence bands of the bulk semiconductors systems. Applying a  $V_{ds}$  Voltage along the wire that shifts the two Fermi Levels of the electrodes, a "Bias Window" is opened (figure 2.2): conduction occurs between the available states of the electrodes and the levels of the molecule. Therefore the choice of the molecule is fundamental designing the conductivity and the whole transport mechanisms of the junction<sup>[22]</sup>.

This type of wire can be indeed useful for many applications by physically and chemically manipulating the molecule: for example, given a  $V_{ds}$  BIAS, a tunable vertical "Gate" Voltage over the molecule can shift HOMO-LUMO levels inside and outside the BW, thus creating on and off states of a Transistor (ON if there is a molecule state for electrons to coherently tunnel at energies between the two Fermi Levels, OFF if there is not).

Differently, if a properly electroluminescent molecule is used, with the right passing current the device will emit photons creating a molecule-based LED with really low power dissipation and manufacturing cost, avoiding heavy metals and rare earth mining.

On the contrary with a photochromic molecule that can undergo to reversible isomers with open/closed conformations if exposed to light (so changing orbitals and so states and so conductivity) the device can switch between high-conductance state (ON) and low-conductance state (OFF), developing photoswitchers and light sensors.

Same happens if the properties of the molecule are chemically changed (or physically, like

in fullerene gas sensors) by the formation of new bonds with external particles, where the wire molecule is used as an anchoring site for a designed guest molecule, building atomic ultrasensitive sensors.

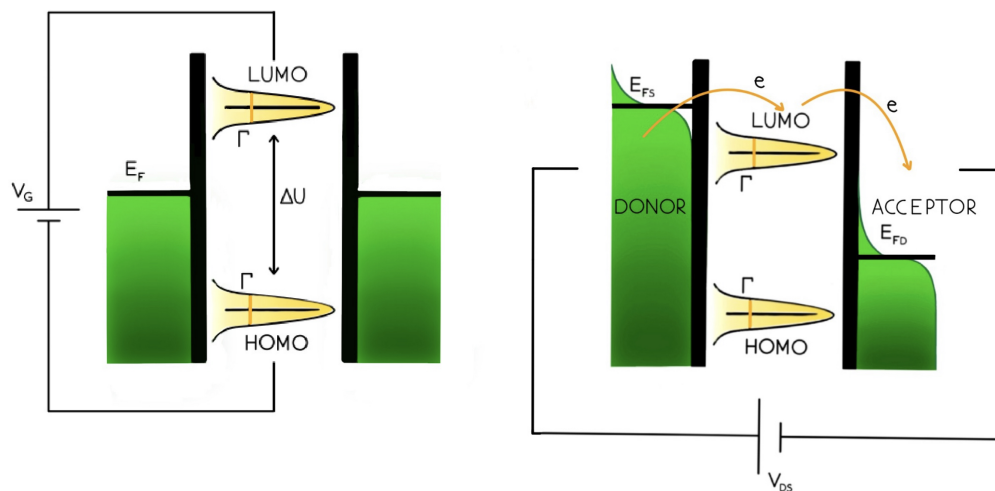


Figure 2.2. Molecule states and their  $\Gamma$  broadening of a SMJ,  $V_g$  modulates levels position w.r.t the  $E_F$  of the electrodes,  $V_{ds}$  creates a bias window that allows transport

## Electrodes

The fabrication of single molecule junctions first goes through the creation of a break-junction<sup>[23]</sup>: a nanometric wire, usually gold for its malleability and high conductance, is processed to shape a nanometric gap on the order of the inter-atomic spacing for guesting the molecule. Since the nanogap is on the order of few nanometers, even best resolution lithography methods are not sufficient for achieve high quality controlled gaps: the two main break-junction techniques used are mechanical and electrical.

In Mechanically Controlled Break Junction (MCBJ) the wire is deposited over a flexible substrate and the gap is achieved precisely bending the layers vertically, in Crack Defined Break Junction (CDBJ) the wire and the holding substrate (with proper elastic strain constant) are horizontally stretched until a cracked gap appears.

Electrical break junctions are created by exploring electromigration in metallic wires: under controlled temperature and feedback controlled voltage ramps, the wire is gradually thinned out by the critical current that flows away the ions, until the formation of the gap.

In all fabrication methods a feedback circuit detects the variations in resistance and stops the processes when the conductance becomes critically low,  $\sim G_0$  for tunnelling current through the air barrier. Bridging the molecule the “ON” conductance state is revealed and so the molecule junction is created.

Generally in the case of gold electrodes and organic molecules the bonds have to be mediated by linkers, thiol anchoring is often used to achieve a strong mechanical, chemisorbed



molecule-electrode connection (structure as figure 2.1): due to gold low compatibility, in order to avoid anchoring groups “contaminations” in the last years graphene electrodes (that exhibit excellent conductive properties due to  $\pi$  aromatic delocalization) have been suggested for their predisposition to more common covalent bonds or  $\pi$ - $\pi$  conjugated ones, ensuring a wider range of manufacturable devices with low cost.

## Linkers

The right choosing in the molecule-electrodes bond is fundamental for ensuring good physical and chemical stability of the systems since the device must guarantee the right endurance from Temperature (Ambient, Voltage..) variations, having the correct Safety Operating Area for the final device: some times specific anchoring groups are needed to achieve better connections.

Apart from its stability, the electric transport of the device is strongly affected by the molecule's coupling: from a quantum prospective given the Hamiltonian of the molecule the solved wavefunctions become from localized HOMO-LUMO levels of the isolated molecule to perturbed mixed solutions with the electronic states of the electrodes, leading to broadened states depending how strong is the chemical bonding. In particular, as shown in figure 2.2, the  $\Gamma$  coupling factor measures and regulates the broadening of the levels: as a general rule if  $\Gamma \gg \Delta U$  there are no "OFF" energies since the molecule's levels are overlapping, meaning strong coupling regime of the systems and higher current. On the contrary, if  $\Gamma \ll \Delta U$  the molecule is weakly bound, meaning not alignment of the orbitals and so low spectral current density.

This is of course a tunable parameter in the device engineering since resonant regimes are amazing for achieving high conductivity of the junction, but not optimal for example to get high ON/OFF ratio for transistors or sensors.

Good linkers can be needed for ensuring the optimal stability and  $\Gamma$  coupling, mixing quantum chemistry with microelectronics and solid state physics.

Below is reported a table 2.3 showing the most common and functional chemical bonds for stability-conductance, both for gold and graphene electrodes: covalent such as sulfur, carbon or amide bonds;  $\pi$ - $\pi$  stacking methods with anthracene and pyrene<sup>[24]</sup> as anchoring groups in graphene.

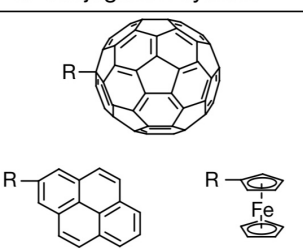
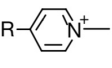
Covalent bonds	Donor-acceptor bonds		Electrostatic interaction
	Lone pair system	$\pi$ -conjugation system	
$\text{R}-\text{S}-\text{Au}$ $\text{R}-\text{N}(\text{H})-\text{Au}$ $\text{R}-\text{C}(\text{H})-\text{Au}$ $\text{R}-\text{C}(\text{H})_2-\text{Au}$ $\text{R}-\text{C}_6\text{H}_4-\text{Au}$ $\text{R}-\text{N}(\text{H})-\text{C}(=\text{O})-\text{G}$	$\text{R}-\ddot{\text{S}}\text{Me}$ $\text{R}-\ddot{\text{Se}}\text{Me}$ $\text{R}-\ddot{\text{P}}\text{Me}_2$ $\text{R}-\ddot{\text{I}}:$ $\text{R}-\text{N}=\text{:}$ $\text{R}-\text{N}\equiv\text{N}:$ $\text{R}-\ddot{\text{N}}\text{H}_2$ $\text{R}-\text{C}_5\text{H}_4\text{N}:$		

Figure 2.3. Most common and versatile chemical bonds for molecular junctions

## 2.3 Beyond gold: graphene electrodes

Gold, while being excellent for manufacturing break-junctions with both mechanical and electrical methods, shows important and not negligible limitations: apart from the previously mentioned restrictions with molecule bonds (forcing the design of proper anchor groups), a real issue is that even with low voltage operating ranges conductance is so high that at room Temperature the high current induces electromigration, damaging and breaking the leads, giving unstable and low endurance devices.

Platinum can be exploited for avoiding electromigration, but it would be too expensive and it would not solve neither the narrow range of available bonds nor another problem of metallic electrodes: bulk screening.

The screening of the applied gate field over the molecule is in fact inevitable since metallic electrodes are necessarily thicker than the bridged molecule, quenching the wanted  $V_g$  Voltage for the molecule.

All these problems can be overcome by graphene sheets used as electrodes<sup>[25]</sup>: Carbon is relative cheap to be processed, monolayer graphene has the same thickness of molecules (so no bulk screening), it avoids metal oxidation, and the  $sp^2$  bonds of the lattice are really robust even far from room Temperature (so no electromigration) while the resonant  $\pi$  bonds of delocalized orbitals guarantee perfect conductance values.

Also, Carbon has wider compatibility with organic molecules, ensuring strong covalent C-C bonds (for example with benzene OPE3 or OPE5 molecules) or  $\pi$ - $\pi$  overlayer anchors very helpful during fabrication.

For this purpose, many break-junction fabrication methods have been developed, such as Dash-Line Lithographic (DLL) method, feedback-controlled electroburning, MCBJ for graphene, graphene-coated copper wires and more.

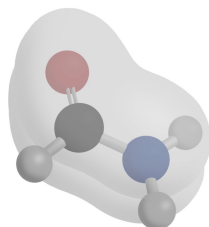


Figure 2.4. Formamide  $\pi$  orbitals

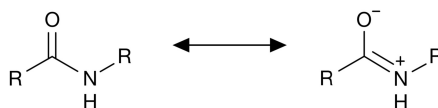


Figure 2.5. Resonance in amide groups

A mention to an amazing linker for graphene, the amide group<sup>[26]</sup>. During the productive processes of graphene nanogaps (if not done in vacuum) the edges of the junctions can oxidize, creating carboxylic groups  $G-C(=O)-OH$  at the tips of the electrodes. If the anchoring molecule is properly designed with amine groups  $R-N(-H)-H$  on its sides, high-yield molecule junctions can be created just putting the carboxylic break-junctions in solution with the amine terminated molecules. Spontaneously, the molecules will bridge the gap exactly as they are designed for, creating amide bonds  $G-C(=O)-N(-H)-R$  with the release of an  $H_2O$  molecule in the solution.

Therefore in addition to being excellent for easily producing single molecular junctions, this linker is optimal for its stability: the C-N bond is quite robust and does not break even far from room temperature, and most importantly it does not allow rotation, avoiding spurious changes in conductance due to orbitals variation. So it not only guarantees high endurance junctions, but it's perfect for electronic transport for presenting  $\pi$  delocalization as graphene and aromatic compounds, figure 2.4, thanks to the resonance between C=O and C-N bonds, figure 2.5: the amide linker is both stable and conductive.

Of course the drawback is that the synthesis of molecules containing two terminal amine groups is relatively difficult and so more expensive in comparison with a  $\pi$ - $\pi$  stacking method or covalent bonds in metal electrodes.

However differently from metal electrodes, in which it is difficult to reach the edges at the atomic level and the uncertainty of the bonding positions of the linkers can affect the whole transport mechanisms, amide anchoring groups give precise sites and so accurate control in fabrication<sup>[27]</sup>.

## 2.4 Electroburning method

One of the methods to obtain graphene break-junctions is the corresponding electromigration technique for metal-based break-junctions from nanowire<sup>[28]</sup>.

As a first step, since usually a SLG could result unstable by folding in on itself, few layers of around 3-18 nm are deposited by mechanical exfoliation of kish graphite over silicon substrate coated with thermal silicon oxide. Notice that few MLGs are still far from graphite so no bulk gate screening is present.

Then gold contacts are patterned with CVD and lithography processes at left and right edges of this multi layers graphene wire, to make contact points for the voltage circuit and to connect the junction with the external integrated circuit, figure 2.6.

In air and at room pressure and temperature, the initial wire conductance is measured, obtaining around  $\sim k\Omega$  resistance. The whole processes is based on voltage ramps that heat the wire with Joule effect, in which local high temperatures break the  $sp^2$  contacts of Carbon that evaporates and mixes to Oxygen in the air.

Firstly the graphene wire is cleaned of impurities with a first voltage ramp which gives a non-linear IV characteristic, red curve on figure 2.7. A subsequent voltage ramp is applied with a constant and continuous increase of 1V/s, that proportionally increases the current (almost constant resistance). As soon as the current drops since some carbon atoms evaporate from Joule effects (narrowing the channel), the voltage bias is turned off and the wire is left to cool for avoiding thermal runaway: the resistance increases, so does the Joule temperature, breaking more bonds and so narrowing the channel that increases even more the resistance, with a diverging loop with no control that can burn the entire wire in nanoseconds.

Then successive voltage ramps are made with the same criteria (more and more shorter since the channel is getting thinner, as the blue arrow shows on 2.7 graph) which slowly consume the wire.

What happens is that despite the Joule heating can be considered uniform along the structure, the temperature gets rapidly dissipated near the gold contacts, while the central part

of the wire gets hotter: here the first break occurs at the edges due to incomplete  $sp^2$  hybridization of C-H bonds.

From atom force microscopy (AFM) scanning it can be seen that statistically the break starts spontaneously on one of the two sides, and then it continues preferably on that side by the dangling bonds, creating at the end asymmetric break-junctions along the perpendicular direction.

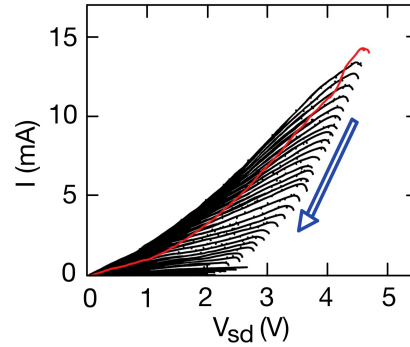
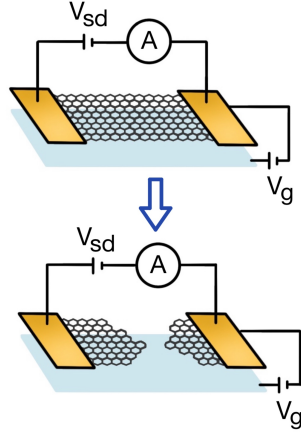


Figure 2.6. Graphene electroburning setup      Figure 2.7. V ramps at controlled constant T

Since it is a surface dependence process, proportional to temperature and evaporation of Carbon, thickness of the MLG is almost unchanged during the process.

When the wire gets resistance values above  $\sim G\Omega$ , meaning nA current due to tunneling through air, nanogap is finally created and the process is over.

Usually gaps of few nanometers are created, but since it can be difficult to obtain accurate measures from AFM characterization, a Simmons model<sup>[29]</sup> is usually used for estimating the gap size, in which the tunnelling current gives an estimation of the width of the air barrier.

High quality stable in time gaps can be created with this technique, that can be done also in vacuum with Carbon sublimation when  $sp^2$  bonds break, avoiding air contaminations<sup>[30]</sup>.

## 2.5 Dash-line lithographic method

Another high-yield low cost method for graphene-based break-junctions relies on a dash-line lithography process<sup>[31]</sup>.

In this case, a SLG is deposited by CVD on copper foils for achieving an high quality pure single layer, and subsequently transferred on a  $\text{SiO}_2$  substrate by a polymethylmethacrylate (PMMA) support frame.

Then, as it happens for electromigration setup, gold contacts at Source and Drain are patterned to connect the wire with the bias voltage and the external integrated circuit. The initial resistance is measured, proportional to the width of the starting wire and around

$\sim k\Omega$  resistance.

An high quality expensive PMMA mask is patterned with an A-B dashed line shape, thanks to precisely controlled electron beam lithography that guarantees best possible resolutions around 5 nm, figure 2.8a.

After, the mask is placed over the SLG setup and by oxygen plasma ion etching, figure 2.8b, common drawbacks of lithography are exploited for the final results: the shadowing effects of lithography, which laterally overconsumes the underlayer of the mask due to backscattering effects can pattern the graphene layer in order to create parallel nanogap by accurately choosing A and B lengths, figure 2.8c.

The B length is fundamental for the designed nanogap size, where for larger B smaller gaps lengths. A instead is wanted as short as possible for getting an higher density of parallel junctions, but if it becomes too low, meaning B/A ratio too high, gaps are not created.

The best compromise found is with  $A = 150$  nm and  $B = 40$  nm.

In fact one of the most useful points of this break-junctions method is the possibility to produce many gaps fabricated in parallel, with excellent reproducibility and stability.

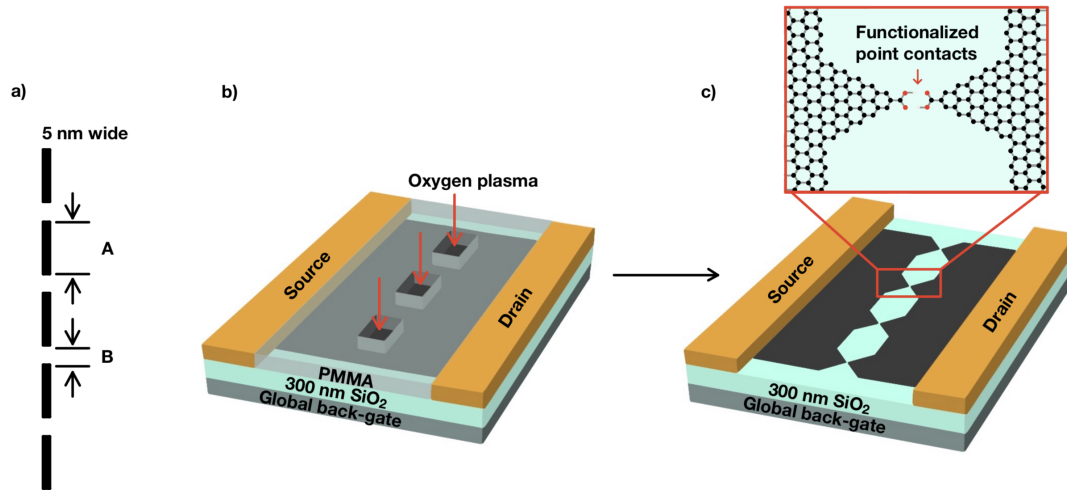


Figure 2.8. Dash-line A-B lithography for parallel junctions, with carboxylic point contacts

Given the strongly oxidizing condition induced by oxygen plasma, carboxylic acid-terminated graphene point contacts arrays are produced at the tips of the nanogaps. With amine or pyridine terminated molecule in solution, many amide linked graphene–molecule–graphene single-molecule junctions (GMG-SMJs) can be made in precised controlled parallel sites, achieving high-yield low cost fabrication parallel junctions.



## Chapter 3

# GMG-SMJ simulations

Once it is known how GMG-SMJ are fabricated, and how conductance works in graphene-based electrodes, it is finally possible to set up simulations based on quite reliable realistic devices, and see which physical mechanisms rule the electronic transport.

Thanks to the QuantumATK software many examples will be made, starting from a simple 2D 9aGNR wire and complicating the geometrical structure step by step until a realistic molecule junction is analyzed.

### 3.1 QuantumATK

Synopsys' QuantumATK® is an integrated platform of electronic and atomic-scale modeling tools written in Python and C++. The atomic scale calculator used in the following simulations is based on Density Functional Theory using numerical LCAO (linear combination of atomic orbitals) basis sets, and with a non-equilibrium Green's function (NEGF) method unique of QuantumATK it is possible to compute nanodevices with nonzero bias between the electrode leads.

In the following simulations, unless otherwise specified, a Fritz-Haber Institute (FHI) pseudopotential is used, with a  $k_c = 9$  sampling grid that provides the best performance-accuracy ratio.

All set parameters are reported below, the other are set by default to 2022.03 version<sup>[M]</sup>.

Calculator	Pseudopotential	Basis set	k-points sampling
LCAO	FHI	DZDP	$n_a = 1, n_b = 1, n_c = 9$
DOS k-points	TS k-points	IV k-points	Pathways k-points
$n_a = 1, n_b = 9$	$n_a = 1, n_b = 9$	$n_a = 1, n_b = 9$	$n_a = 1, n_b = 9$

## 3.2 9aGNR

The first simulated device is an armchair graphene nanoribbon with  $N=9$  width atoms.

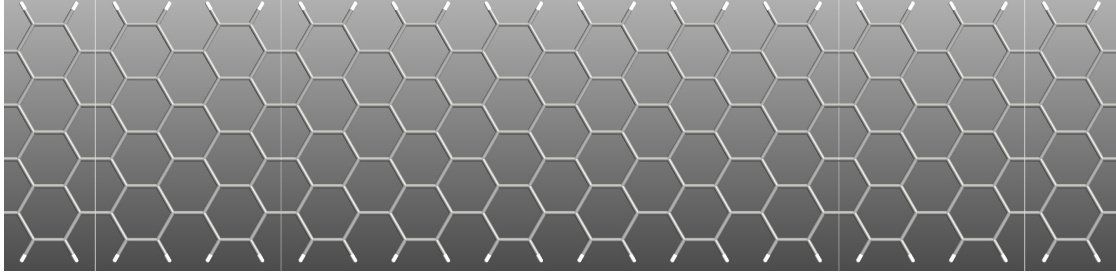


Figure 3.1. Graphene armchair  $N=9$  nanoribbon device, regions from left to right: left lead periodicity, left lead, central scattering region, right lead, right lead periodicity

In all devices the electronic transport will be simulated from left lead, passing through the central region, to the right lead. The outermost left and right regions of figure 3.1 represent the leads periodicity, meaning semi-infinite periodic non-relaxing contacts. If leads regions, also called screening regions, are shorter than the actual (physical) screening length of the system, spurious scattering may take place at the contacts-lead interfaces. This may give rise to poor convergence of the self-consistent calculation and inaccurate results in finite-bias calculations, so for this reason all the simulations will have leads twice as long as their periodicity.

The density of state of this device is expected to be exactly as the one calculated in 1.28 graph: it is actually slightly different, figure 3.2, due to lower  $k$ -sampling points for a performance-accuracy compromise (a LCAO device simulation may last more than several days).

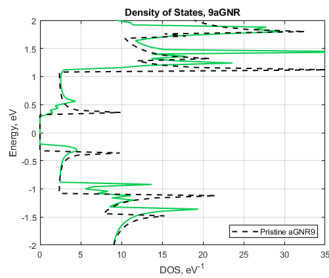


Figure 3.2. 9aGNR DOS

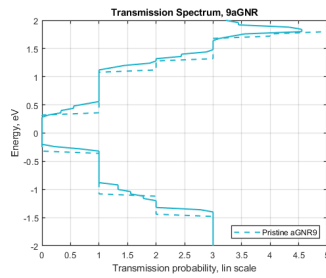


Figure 3.3. 9aGNR TS

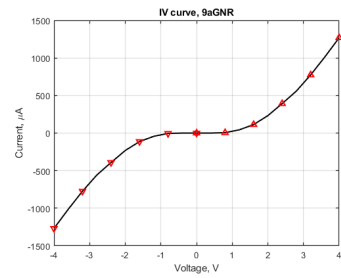


Figure 3.4. 9aGNR IV

For the same reason also the TS of figure 3.3 is not entirely accurate, but it is still possible to recognize the staircase behaviours and so the quantized conductance that produces a tremendously high current, around mA, figure 3.4. Since the device is symmetric, a  $V_{ds} = \pm 4$  V covers the entire  $[-2, 2]$  eV range giving a symmetric IV characteristic.



### 3.3 Benzene with 9aGNR electrodes

The first graphene-based simulated SMJ is a benzene ring with 9aGNR electrodes.

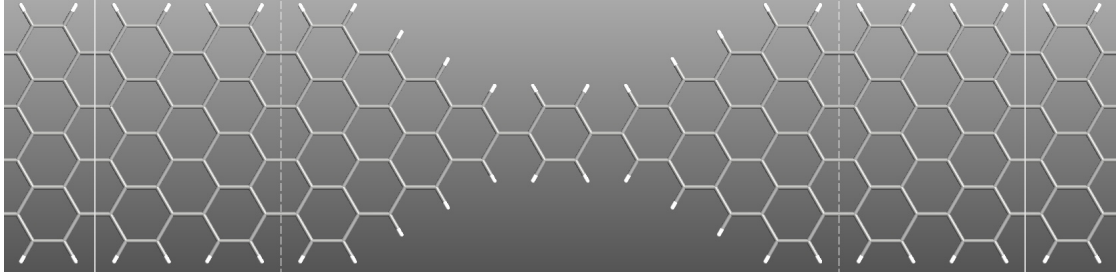


Figure 3.5. Benzene 9aGNR-based single molecule junction

The device is not too different from the graphene wire, it is basically a choked GNR so same DOS scale is expected. For simplicity all simulated devices will be symmetric, meaning same left and right electrodes. For the nomenclature, same as figure 2.1, it will be called *electrode* the lead and tip region, and *molecule* the molecule with (if present) linkers. Starting from the density of state it can be clearly seen from 3.6 graph that from the sum of left and right electrodes (so 2 times electrodes DOS) and the Benzene levels, the total DOS is shown, presenting mixed characteristics.

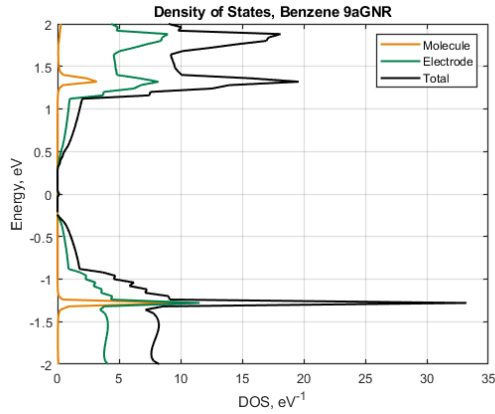


Figure 3.6. Benzene aGNR-SMJ DOS

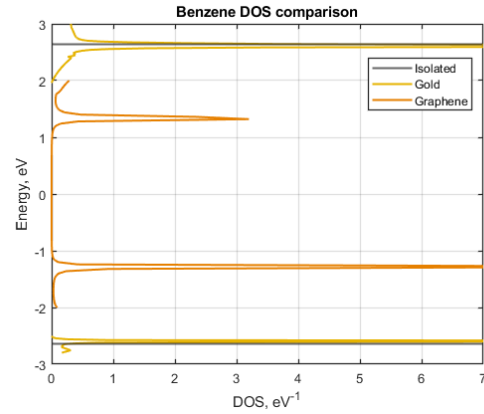


Figure 3.7. Benzene DOS comparison

The electrode DOS is quite similar to the GNR one, with same energy gap: modulating the width of the graphene electrode, a designed gap can be tuned for quenching unwanted molecule states near zero energy, resulting in tremendously low OFF current at zero bias. For the Benzene DOS, the first HOMO-LUMO levels are present in low bias operating range  $[-2, 2]$  eV, around  $\pm 1.3$  eV. Figure 3.7 shows a comparison with a SMJ with gold

contacts (structure of figure 2.1), levels around  $\pm 2.6$  eV, and the isolated benzene ring at slightly more. As expected since an high coupled system means a lowering of H-L gap and broadening of the states, graphene-based junction is better coupled than the basically not coupled gold, in which a really high voltage is needed for allowing transport, around 5 V. The transmission spectrum, figure 3.8, shows exactly the broadened molecule levels that contributes to the conduction, and the log scale, 3.9, shows that no states are present in the electrodes gap region, guaranteeing an high ON/OFF current ratio.

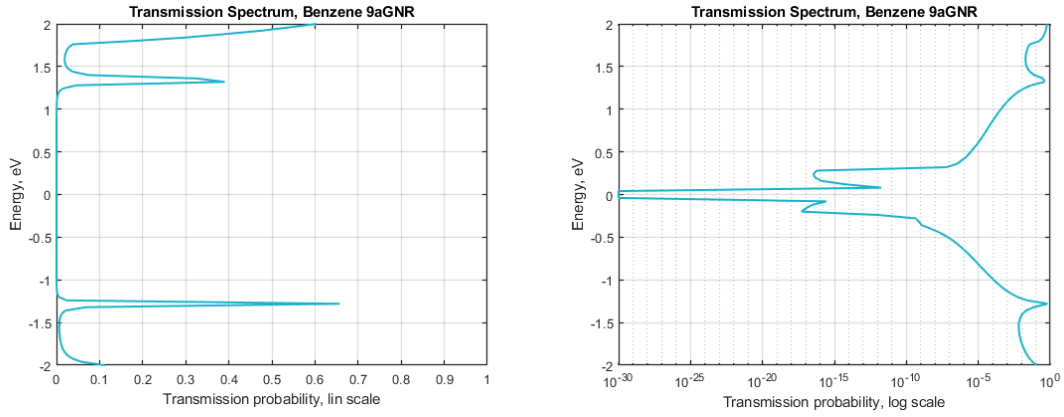


Figure 3.8. Benzene aGNR-SMJ TS, lin scale Figure 3.9. Benzene aGNR-SMJ TS, log scale

Integrating the TS with a  $V_{ds} = 4$  V needed to cover the  $[-2, 2]$  eV operating range, an increasement of the current is appreciable when the benzene states enter in the bias windows, around 3 V, figure 3.10.

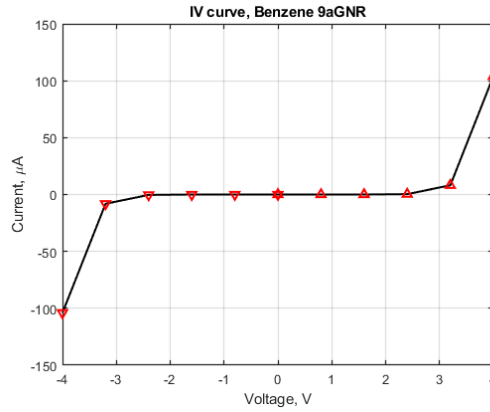


Figure 3.10. Benzene aGNR-SMJ I-V characteristic

The electronic path is shown to visualize the open and closed channel for the two states of a possible transistor, figure 3.11 and 3.12.

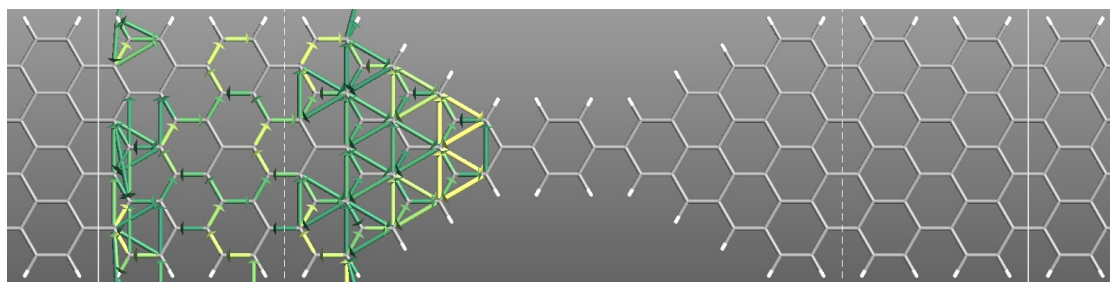


Figure 3.11. Benzene 9aGNR electron pathways, OFF state, 0 eV

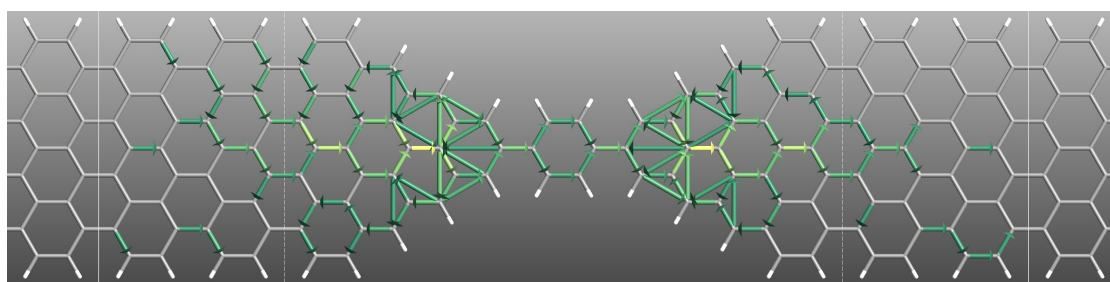


Figure 3.12. Benzene 9aGNR electron pathways, ON state, HOMO =  $-1.28$  eV with  $T=0.66$

### 3.4 OPE3 with 9aGNR electrodes

The second molecule is an oligo-phenylene-ethynylene OPE3, with 9aGNR electrodes.

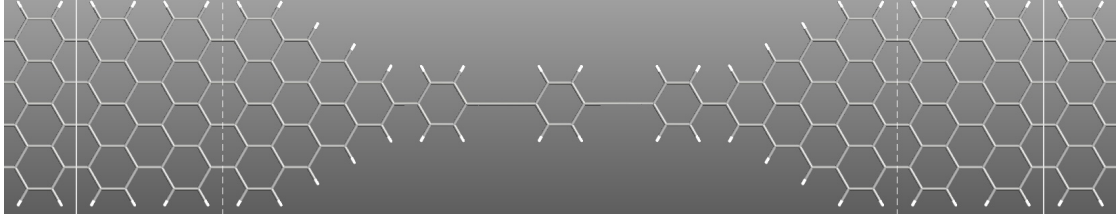


Figure 3.13. OPE3 9aGNR-based single molecule junction

Using the same geometry an OPE3 is attached with  $sp^2$  bonds at left and right electrodes. This molecule, with 3 phenyl functional groups connected by two ethynyl functional groups, allows large  $\pi$  delocalized orbitals along the transport direction.

The density of states will have the same energy gap of the previous device, changing the peaks of the molecule: the general rule is that with more atoms, so more orbitals, there will be more energy levels in the same bias window. Figure 3.14 shows the first 2 HOMO and LUMO states at around  $\pm 1$  eV and  $\pm 1.6$  eV.

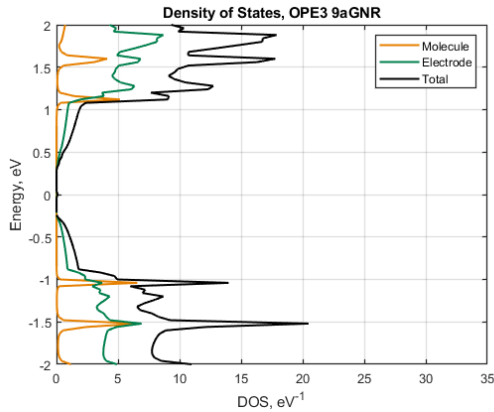


Figure 3.14. OPE3 aGNR-SMJ DOS

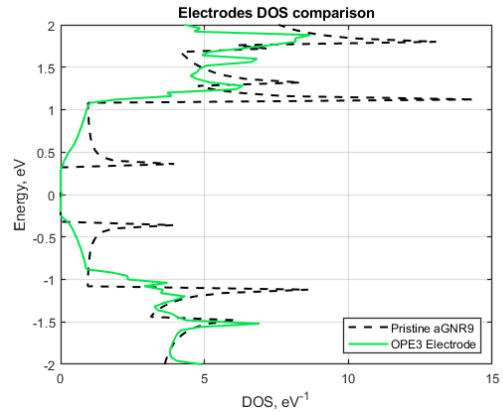


Figure 3.15. Electrode DOS comparison

Figure 3.15 shows how the whole left electrode density of states differs from its correspondent in length nanoribbon: despite the "triangular" shape of the electrode, the DOS presents same gap and almost same values, besides the  $1/\sqrt{E}$  that are typical of pristine 2D systems.

This is quite interesting as a design parameter in the break-junction fabrication since it allows accurate predictions of the electrodes just looking at the main contact width.

The transmission spectrum will follow the molecule properties and its peaks, figure 3.16, where of course the transmission probability of each state can be different depending on the correspondent orbitals: in this case HOMO-1 and LUMO+1 contribute more than HOMO and LUMO. The logarithmic scale of figure 3.17 shows that when first electrodes states are available, around 0.2 eV, tunneling current proportional to the length of the molecule is possible, up to  $T = 10^{-14}$  against  $T = 10^{-12}$  of benzene since the air barrier width is  $\sim 4$  times wider.

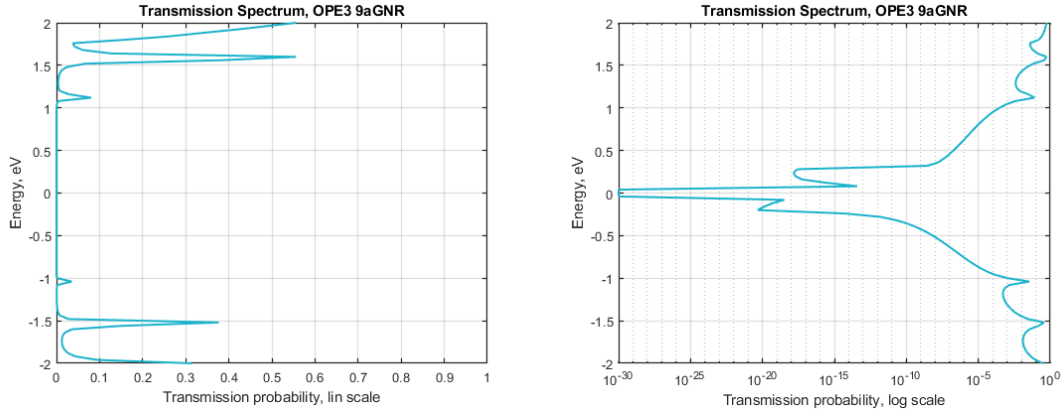


Figure 3.16. OPE3 aGNR-SMJ TS, lin scale    Figure 3.17. OPE3 aGNR-SMJ TS, log scale

The current, figure 3.18, will be similar to the Benzene one, slightly less since the overall molecule is longer: as expected the conductance is inversely proportional to the length of the wire, resulting to  $\sim 80 \mu\text{A}$  against  $\sim 100 \mu\text{A}$  where the whole BW is integrated.

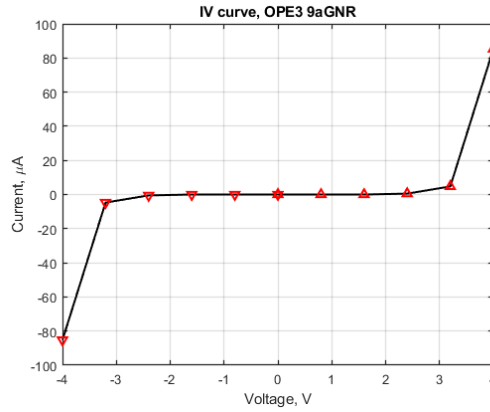


Figure 3.18. OPE3 aGNR-SMJ I-V characteristic

The electronic path is shown to visualize the open and closed channel for the two states of a possible transistor, figure 3.19 and 3.20.

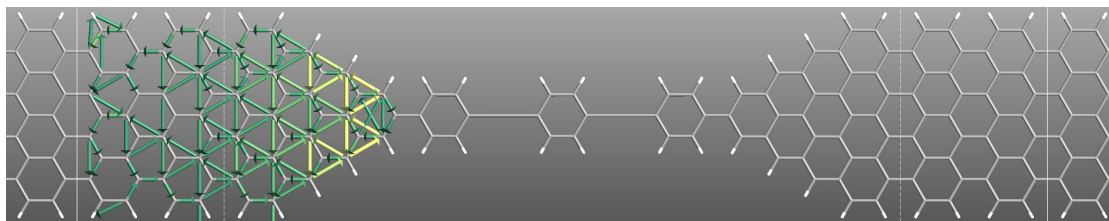


Figure 3.19. OPE3 9aGNR electron pathways, OFF state, 0 eV

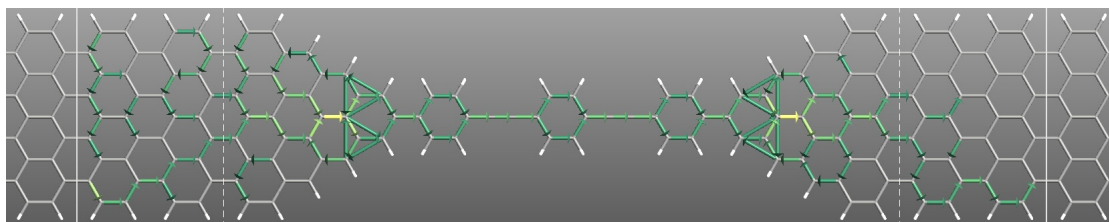


Figure 3.20. OPE3 9aGNR electron pathways, ON state, LUMO+1 = 1.6 eV with T=0.56

### 3.5 OPE5 with 9aGNR electrodes

The third molecule is the oligo-phenylene-ethynylene OPE5, with same 9aGNR electrodes.

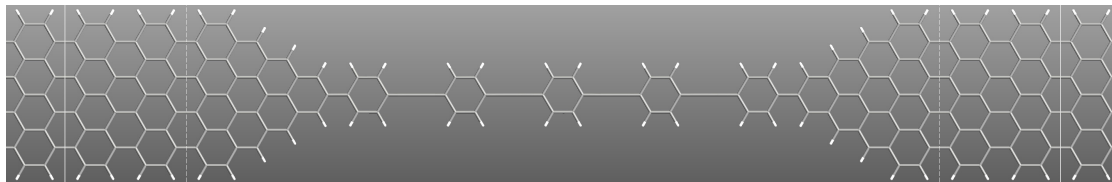


Figure 3.21. OPE5 9aGNR-based single molecule junction

OPE5 has 5 phenyl functional groups connected by four ethynyl functional groups, still with  $\pi$  delocalization along the transport axis that creates an electronic cloud above the whole 2D junction.

While electrodes DOS is almost the same since they always feel the same aromatic phenyl group with  $sp^2$  bond, the total DOS is influenced by the new peaks of the molecule, figure 3.22.

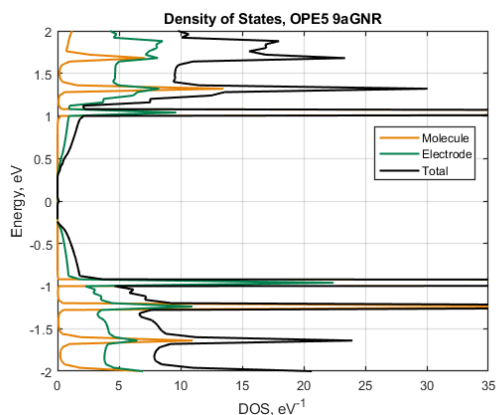


Figure 3.22. OPE5 aGNR-SMJ DOS

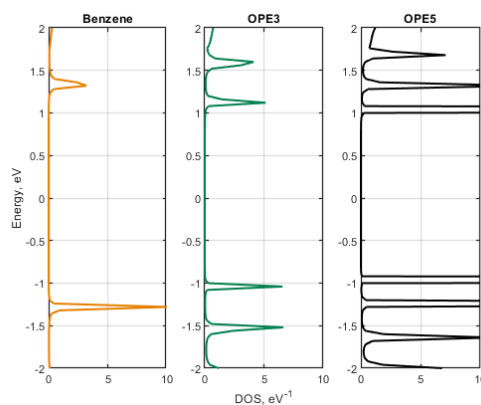


Figure 3.23. Molecule DOS comparison

What happens is that increasing aromatic rings, the number of peaks increases, lowering the HOMO-LUMO gap and with broadening that depends on the coupling of the system, figure 3.23 shows a comparison. In this case up to HOMO-2 and LUMO+2 states are present in the BW, with slightly broadening due to weak coupling regime. Notice in fact that more peaks does not mean specifically more current, if the coupling is weak conductance is ruled by hopping transport: in this case is weaker than before since longer molecule means higher transmission time. The choice of the molecule is therefore fundamental in the engineering of the molecular junction. Consider also that all these molecules

are subject to possible rotations along the transport direction, meaning no more planar systems and so breaking the  $\pi$  electronic cloud above graphene, unfortunately lowering unpredictably the conductance.

TS of figure 3.24 shows the low broadened peaks, while logarithmic TS of figure 3.25 shows that tunneling current for the first populated electrode states is further decreased to  $T = 10^{-15}$  since OPE5 is longer than OPE3.

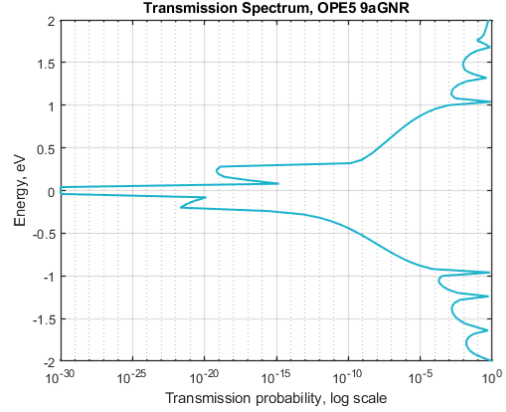
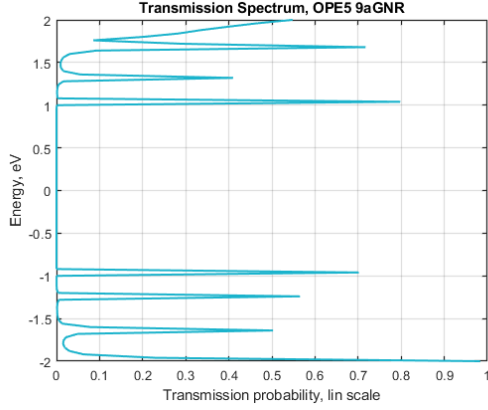


Figure 3.24. OPE5 aGNR-SMJ TS, lin scale      Figure 3.25. OPE5 aGNR-SMJ TS, log scale

As predicted, the current will be lower, respecting the typical behavior of the OPE family in literature. Remember that the device is symmetric, so a  $V_{ds} = +4$  V bias integrated the same BW as  $V_{ds} = -4$  V voltage, changing only the transport direction so the sign of the current.

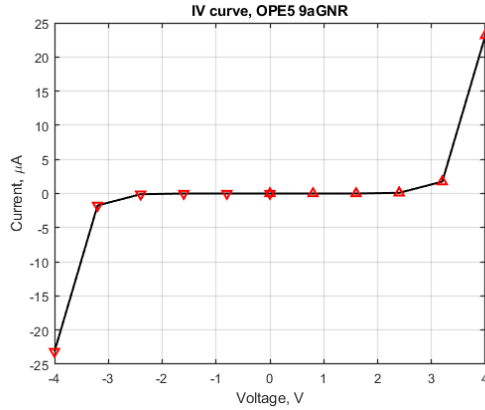


Figure 3.26. OPE5 aGNR-SMJ I-V characteristic

The electronic path is shown to visualize the open and closed channel for the two states of a possible transistor, figure 3.27 and 3.28.



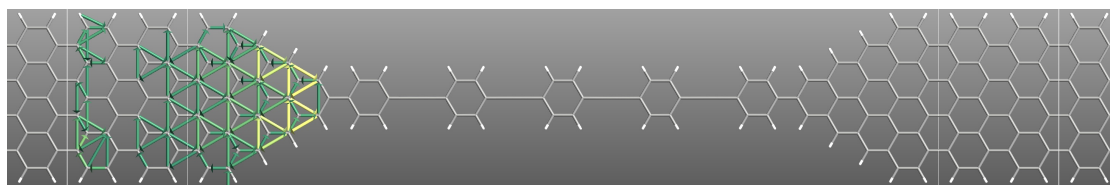


Figure 3.27. OPE5 9aGNR electron pathways, OFF state, 0 eV

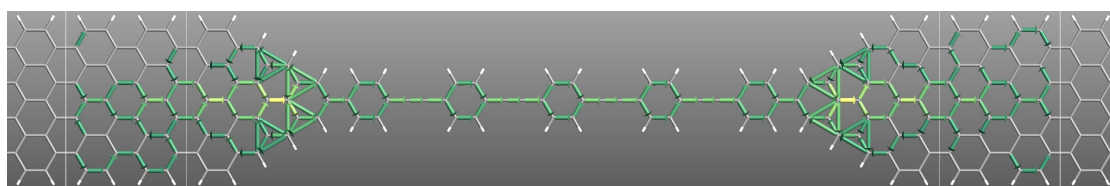


Figure 3.28. OPE5 9aGNR electron pathways, ON state, LUMO = 1.04 eV with T=0.8

### 3.6 OPE3 with graphene electrodes

The fourth device is an OPE3 with large graphene electrodes from real break-junction.

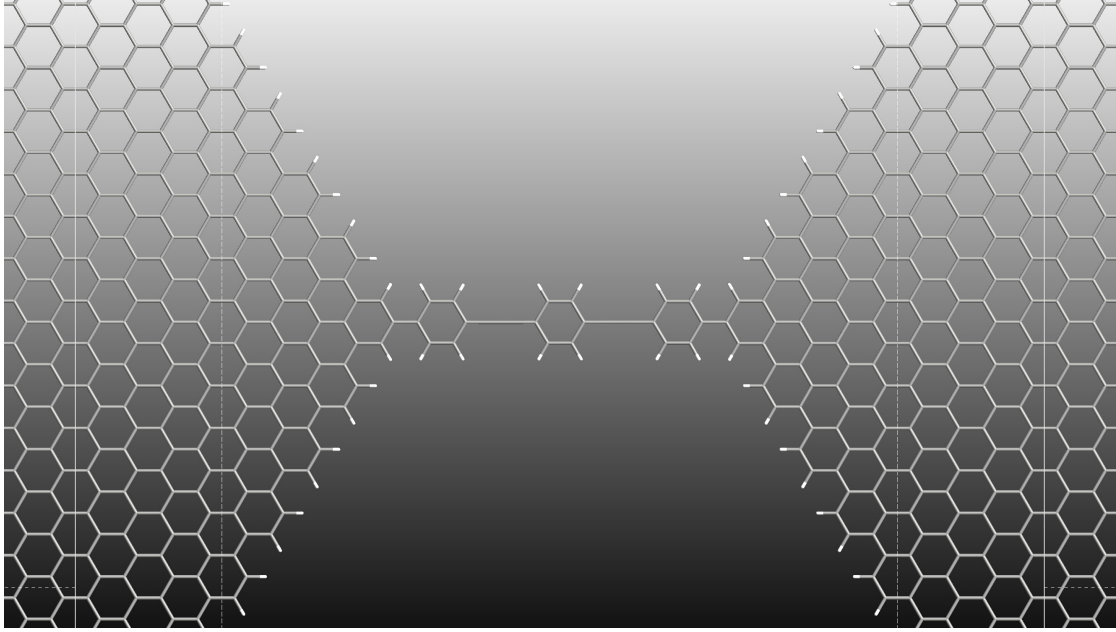


Figure 3.29. OPE3 graphene-based single molecule junction

This time no hydrogen passivations are present in the leads, as happens in parallel break-junctions made from DLL method. This time the electrodes DOS, figure 3.30, recalls the TS of graphene sheet of figure 1.10: as said for the 9aGNR leads, to predict the whole

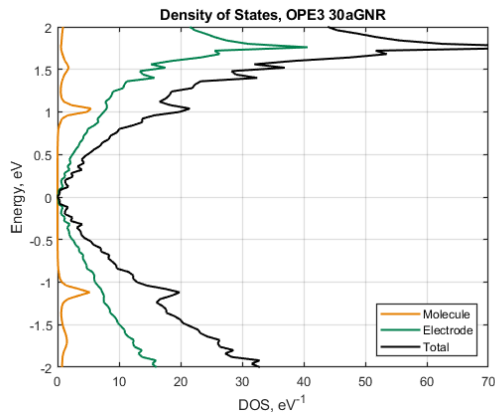


Figure 3.30. OPE3 GMG-SMJ DOS

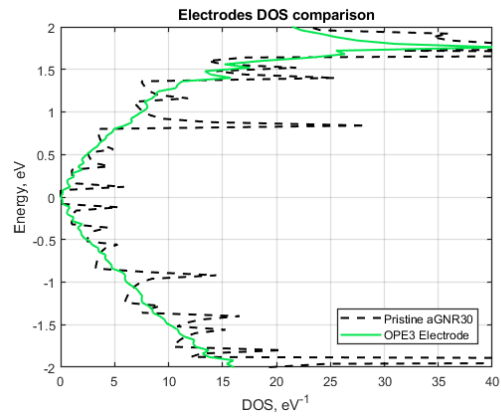


Figure 3.31. Electrode DOS comparison

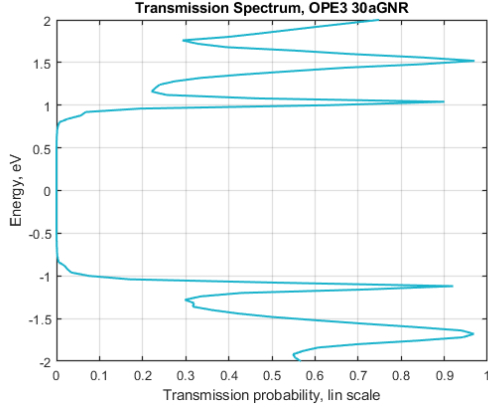


Figure 3.32. OPE3 GMG-SMJ TS, lin scale

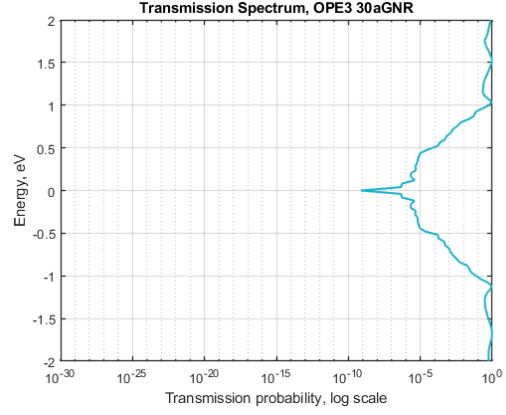


Figure 3.33. OPE3 GMG-SMJ TS, log scale

electrode DOS (considering the not analytical DOS of the triangular shape of the tip), an estimation from its analogous aGNR ( $N=30$  in this case) can be made: also here  $1/\sqrt{E}$  peaks are lost, figure 3.31, but with equivalent in length ribbon the same scale (and gap) is predicted. In TS of figure 3.32 the  $\pm 1$  eV and  $\pm 1.6$  eV OPE3 states are present, with more broadening due to high coupling of the system from low H passivation and an overall higher  $\pi$  delocalization.

The not precisely zero gap in electrodes as happens in pristine 30aGNR allows  $T = 10^{-9}$  tunneling current through the OPE3 length, figure 3.33. It is not the same as the 9aGNR device ( $T = 10^{-14}$ ) since TS does not measure the single electron probability to pass the barrier, but it weights the total transmission from the all occupied states of the electrode DOS. Since broadening is higher, smoother IV characteristics is given, figure 3.34.

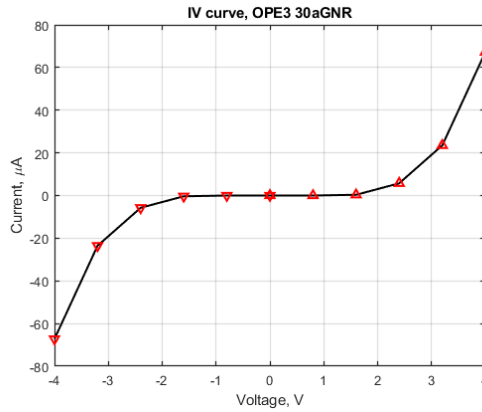


Figure 3.34. OPE3 GMG-SMJ I-V characteristic

The electronic path is shown to visualize the open and closed channel for the two states of a possible transistor, figure 3.35 and 3.36.

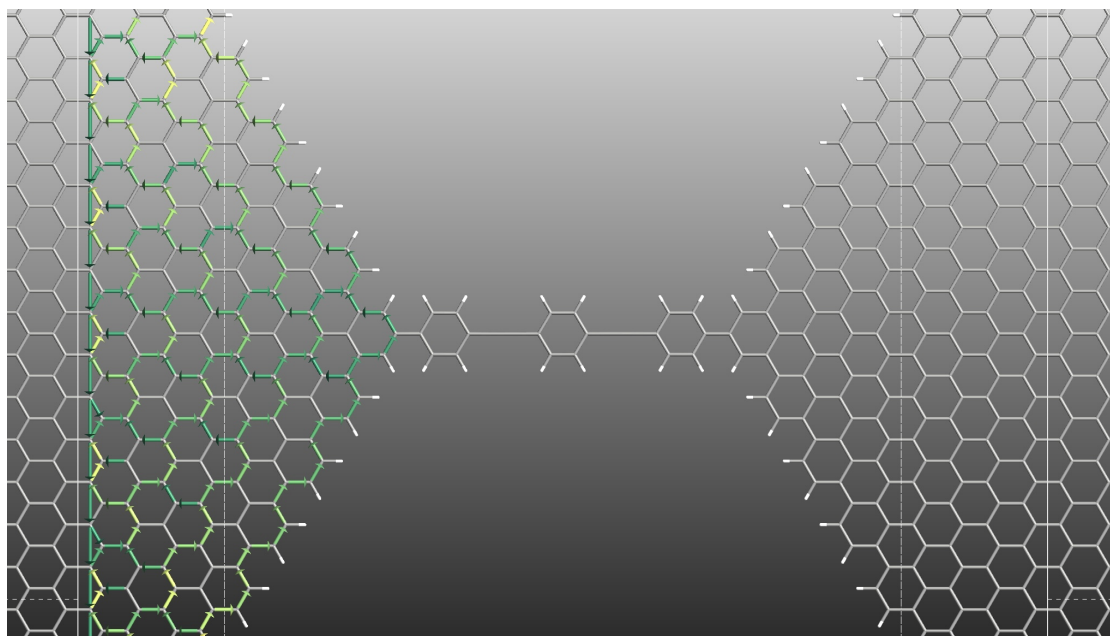


Figure 3.35. OPE3 GMG electron pathways, OFF state, 0 eV

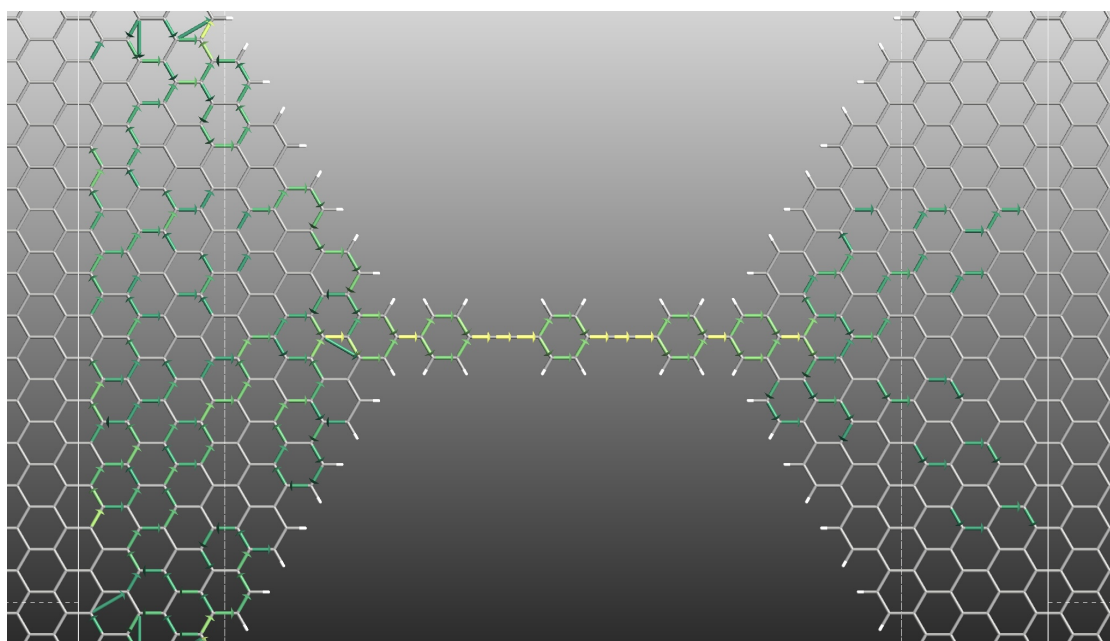


Figure 3.36. OPE3 GMG electron pathways, ON state, HOMO-1 =  $-1.68$  eV with  $T=0.97$

### 3.7 OPE5 with graphene electrodes

The fifth device is the OPE5 with large graphene electrodes from real break-junction.

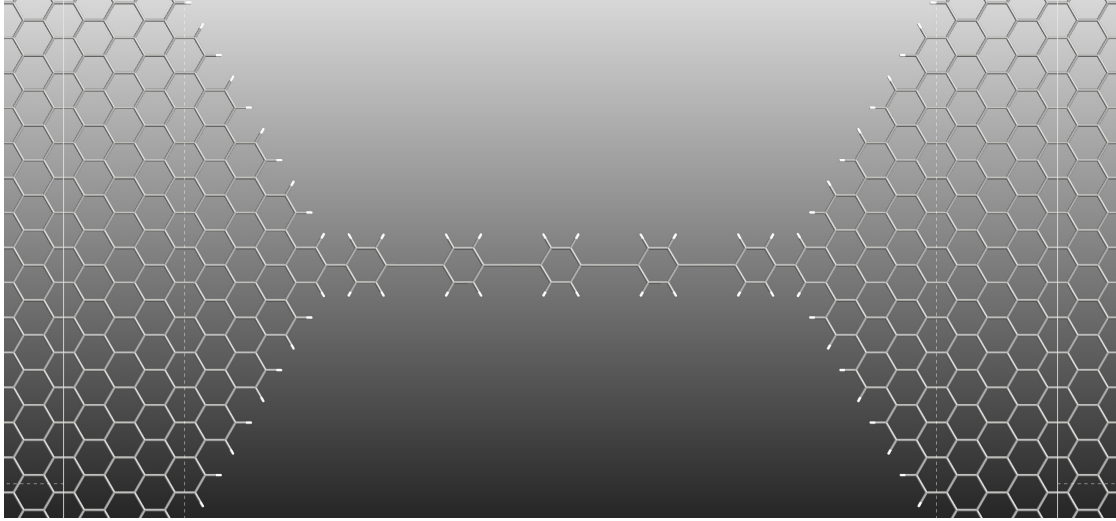


Figure 3.37. OPE5 graphene-based single molecule junction

The density of states is exactly as can be expected: same electrode DOS of 3.30, with more peaks than OPE3-GMG and at the same time more broadening than OPE5-9aGNR, figure 3.38. From the 3.39 comparison it can be clearly seen that experimentally large graphene electrodes gives high coupling for the molecule states, both for OPE3 and OPE5.

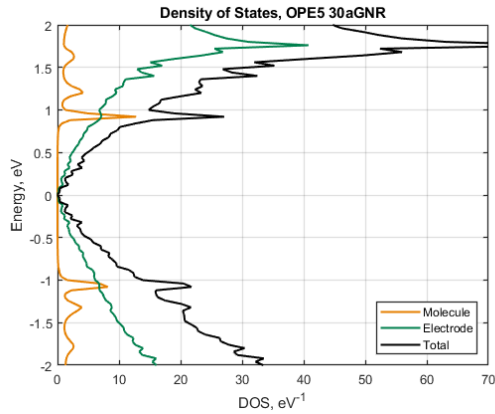


Figure 3.38. OPE5 GMG-SMJ DOS

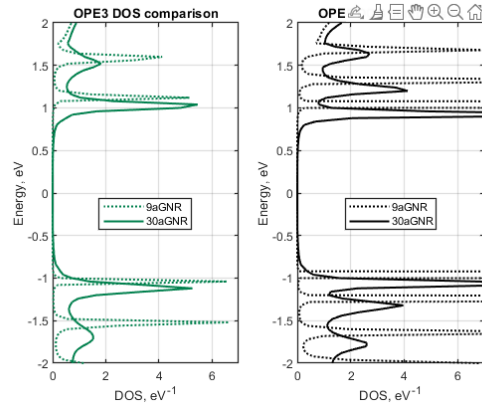


Figure 3.39. OPE junctions DOS comparison

So also in this case TS is made by broadened states, keeping the 3 peaks of OPE5, figure

3.40. Notice that graphene electrodes usually do not shift the molecule Fermi energy, something quite present with gold contacts, that can required a backgate  $V_{BG}$  bias to go to the right operating point.

In the log scale, figure 3.41, first occupied states in the electrodes tunnel with a transmission  $T = 10^{-11}$ , slightly lesser than previous  $T = 10^{-9}$  since OPE5 is longer.

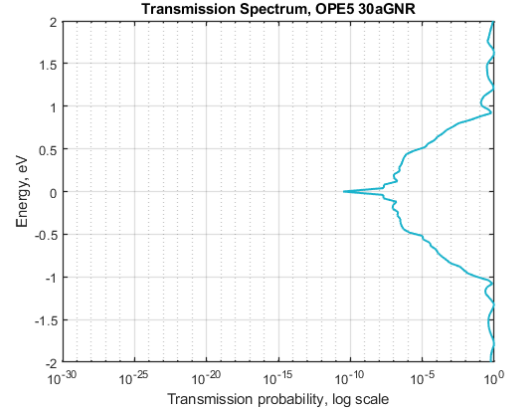
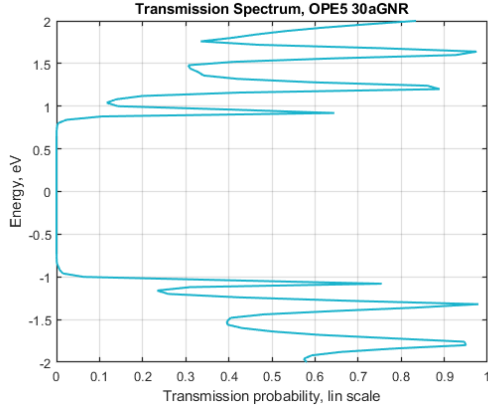


Figure 3.40. OPE5 GMG-SMJ TS, lin scale      Figure 3.41. OPE5 GMG-SMJ TS, log scale

For the current, figure 3.42, while for OPE3 the maximum integrated BW always gave around  $80 \mu\text{A}$ , for OPE5 is around  $25 \mu\text{A}$ , with smoother curve than OPE5-9aGNR 3.26 thanks to high coupling.

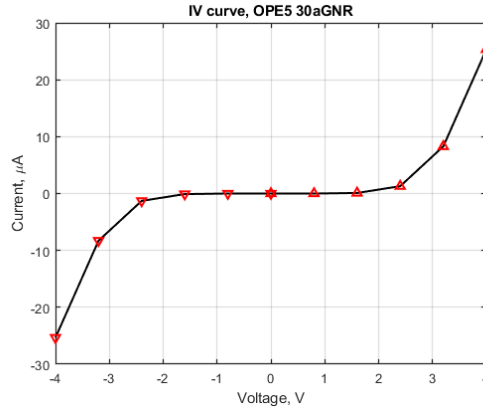


Figure 3.42. OPE5 GMG-SMJ I-V characteristic

The electronic path is shown to visualize the open and closed channel for the two states of a possible transistor, figure 3.43 and 3.44.

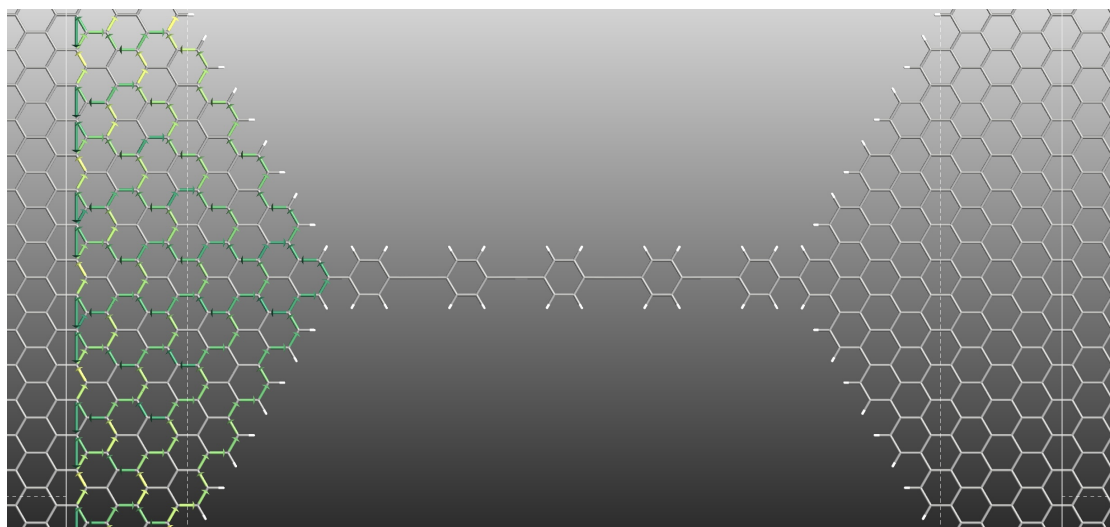


Figure 3.43. OPE5 GMG electron pathways, OFF state, 0 eV

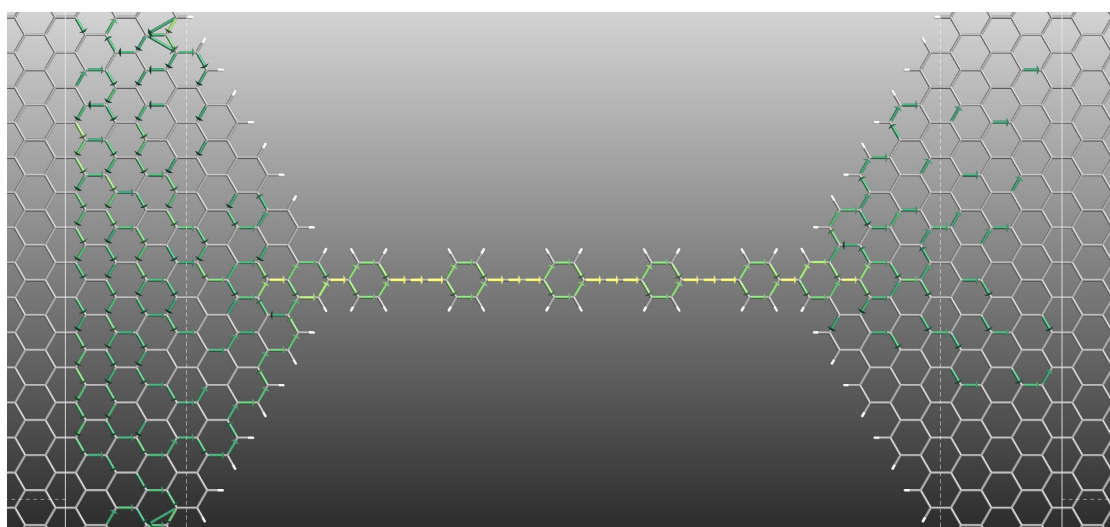


Figure 3.44. OPE5 GMG electron pathways, ON state, HOMO-1 =  $-1.32$  eV with  $T=0.98$

### 3.8 OPE3 with amide linkers and graphene electrodes

The sixth device is the OPE3 linked by amide groups to the large graphene electrodes.

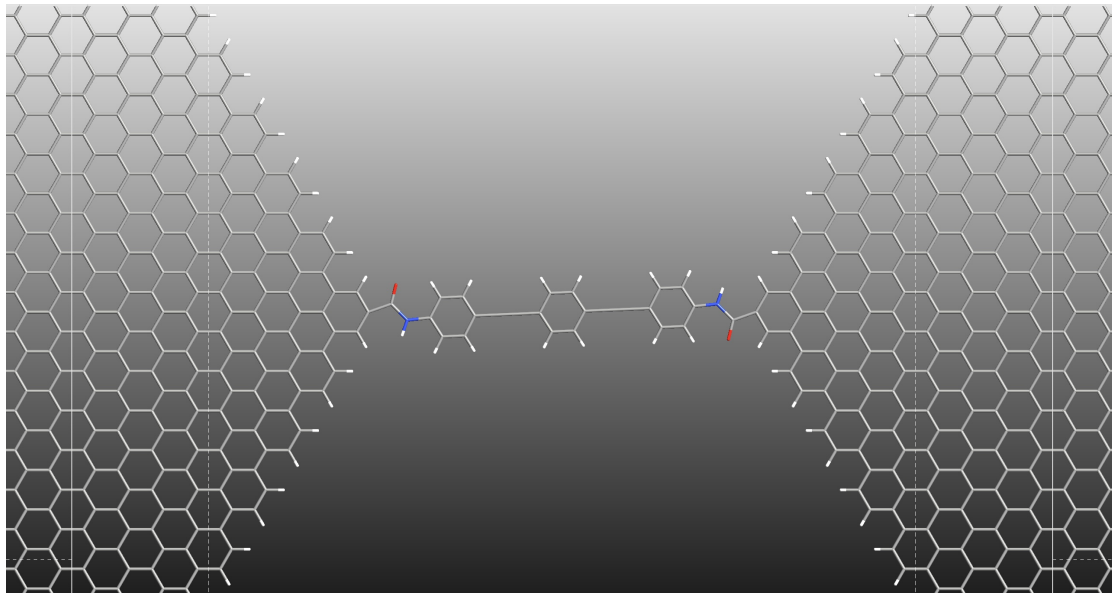


Figure 3.45. OPE3 amide-linked graphene-based single molecule junction

Now the OPE3 molecule is bridged to the junction by amide linkers, possible if oxidized tips that create carboxylic groups are connected to designed amine terminated molecules. These strong anchoring groups avoid spurious rotations due to N-C bond, guaranteeing stability and planar  $\pi$  delocalization (N-C=O resonance) along the entire junction.

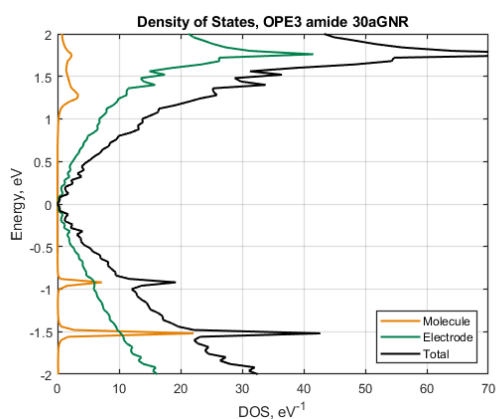


Figure 3.46. OPE3+amide GMG-SMJ DOS

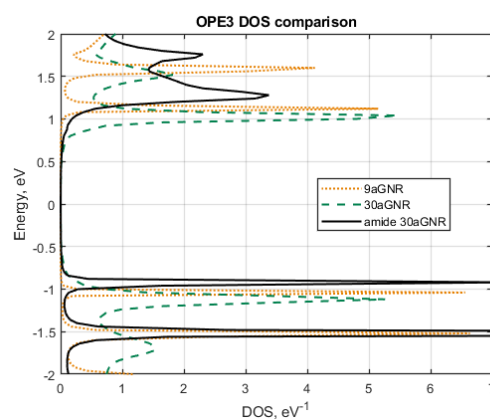


Figure 3.47. OPE3 DOS comparison



The simulation shows that amide linkage creates low coupled HOMO levels and broadened LUMO states, probably due to Nitrogen orbitals contribution, figures 3.46 and 3.47.

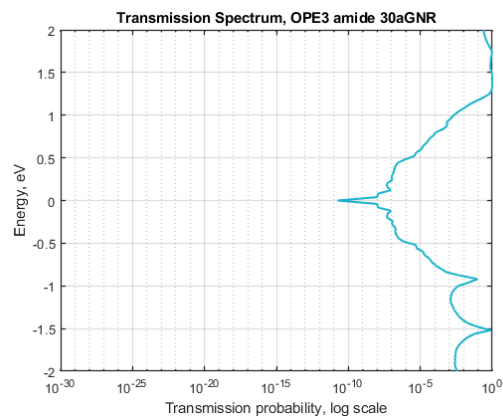
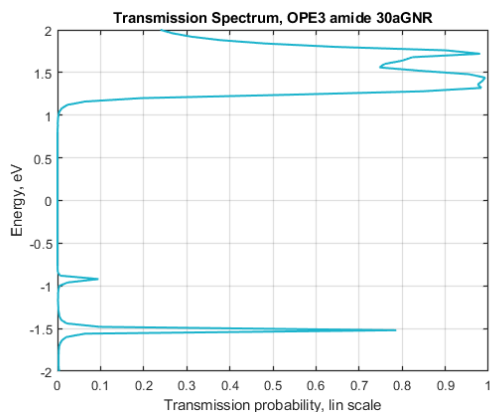


Figure 3.48. OPE3+amide GMG TS, lin scale Figure 3.49. OPE3+amide GMG TS, lin scale

It is also shown in the TS plot, figure 3.48, in which the two LUMO states of OPE3 are basically merged, giving high diffusive current contribution, while HOMO levels have weak coupling regime: also logarithmic plot, figure 3.49, shows a pit between HOMO states.

Of course a backgate bias can be engineered to set the device in the designed operating point.

The overall current is lower than without linkers, figure 3.50, but remember that without amides the rotations can give even low unpredictable current.

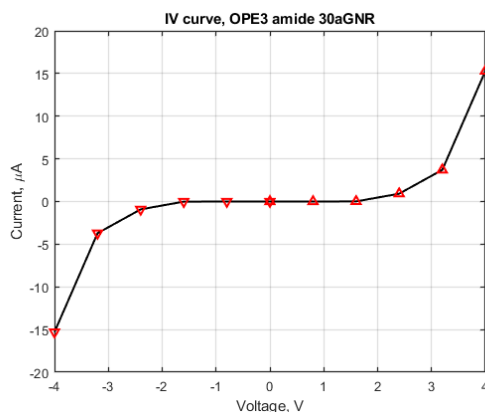


Figure 3.50. OPE3+amide GMG-SMJ I-V characteristic

The electronic path is shown to visualize the open and closed channel for the two states of a possible transistor, figure 3.51 and 3.52.

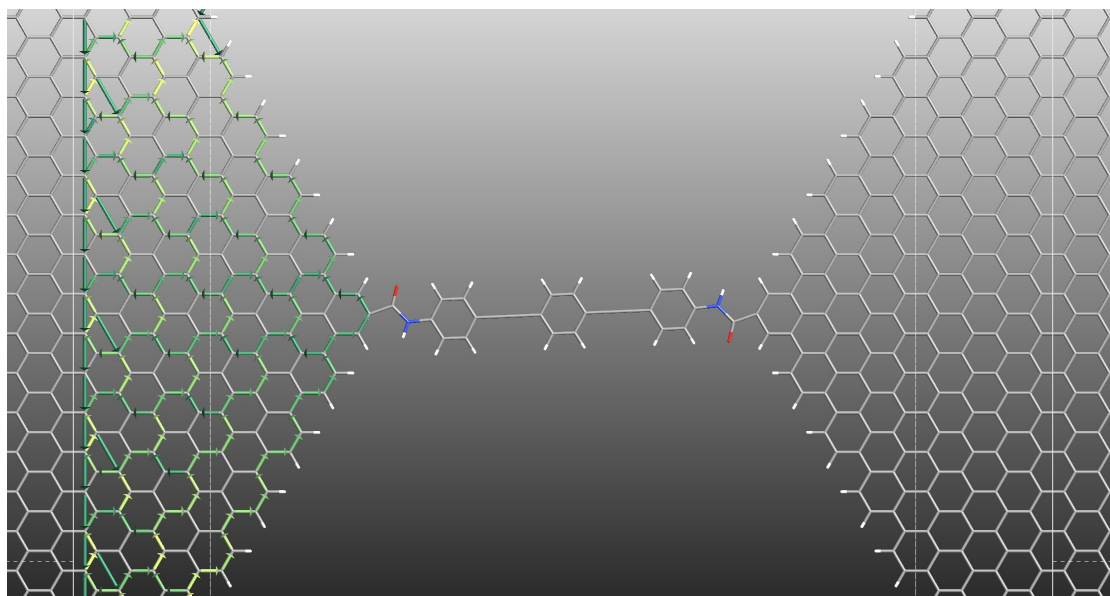


Figure 3.51. OPE3+amide electron pathways, OFF state, 0 eV

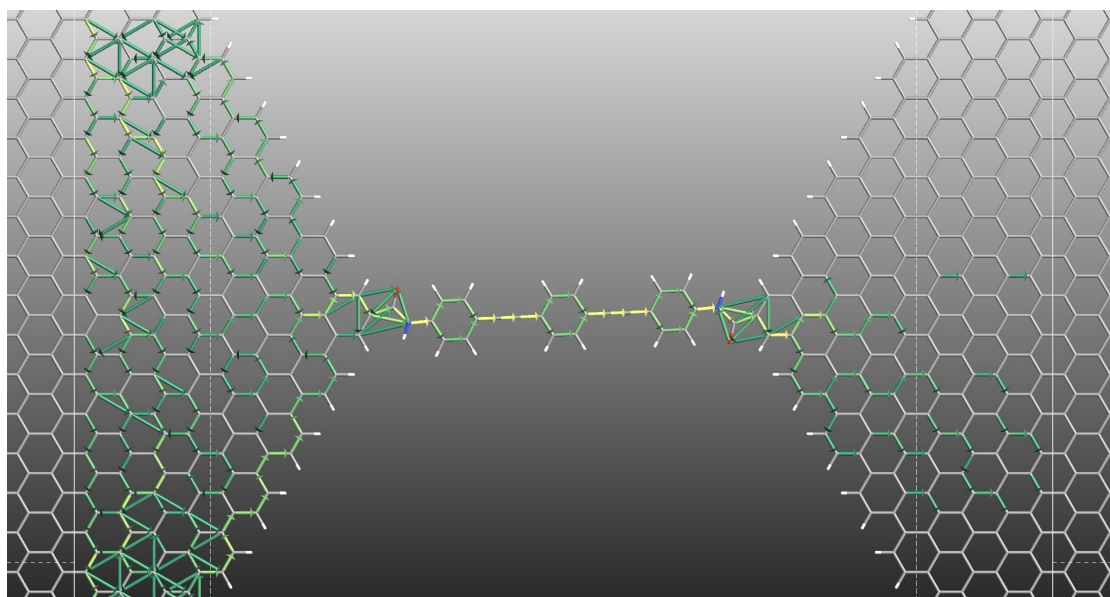


Figure 3.52. OPE3+amide electron pathways, ON state, HOMO-1 =  $-1.52$  eV with  $T=0.78$

### 3.9 OPE5 with amide linkers and graphene electrodes

The seventh device is OPE5 linked by amide groups to the large graphene electrodes.

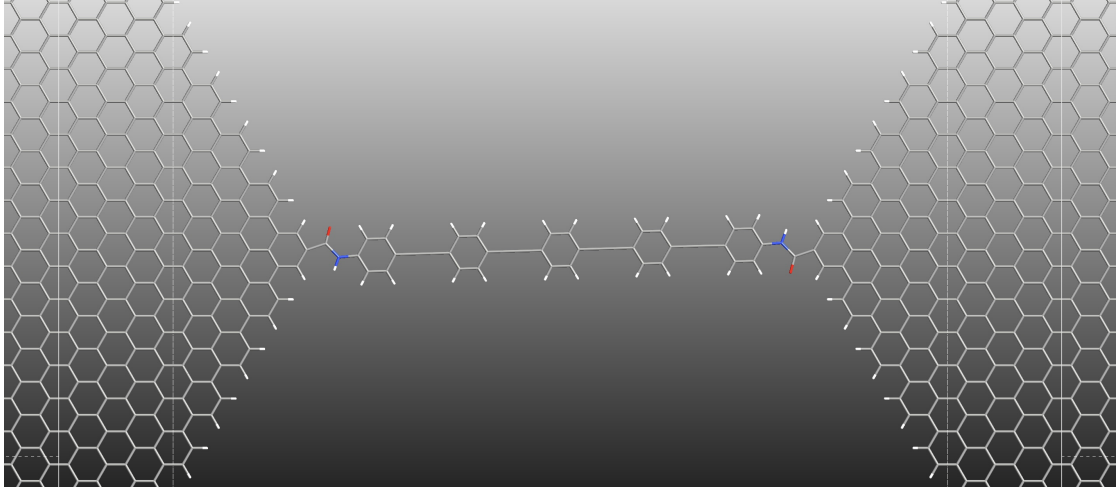


Figure 3.53. OPE5 amide-linked graphene-based single molecule junction

The fabrication process is the same as the previous device since same bonds are involved. The junction is completely planar and large electrodes are high reservoirs of possible conductive states: electrode DOS is not changed, figure 3.54, while the 3 peaks of OPE5 in the  $[-2,2]$  eV range are modulated by amide orbitals.

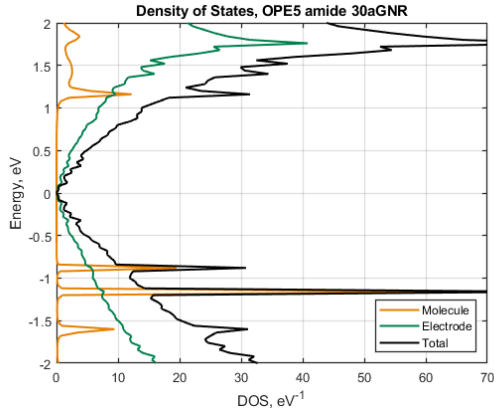


Figure 3.54. OPE5+amide GMG DOS

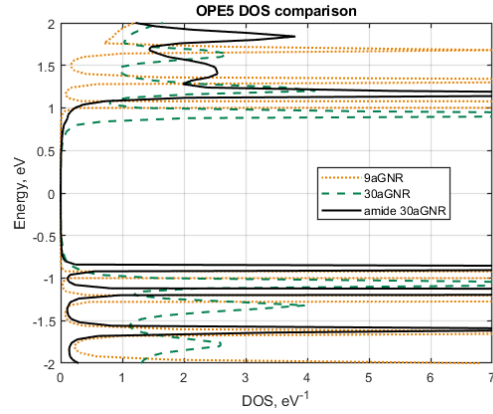


Figure 3.55. OPE5 DOS comparison

Figure 3.55 shows the DOS comparison of OPE5 when it is bridged to 9aGNR, with low coupling but still H-L gap reduced from isolated molecule; high coupling with large

electrodes and H-L gap significantly reduced; and now with amide linkages that isolate HOMO levels and broaden the LUMO ones.

So due to amides the transmission spectrum will suggest coherent tunneling across all LUMO states and hopping transport in the HOMO levels, figure 3.56.

Log scale, figure 3.57, shows how  $T$  drastically drops between HOMO states. It also shows the low zero bias current (at 0 eV), with  $T = 10^{-12}$ , slightly less than the  $T = 10^{-11}$  shorter OPE3+amide, of course both lower than the respective amide-free junctions.

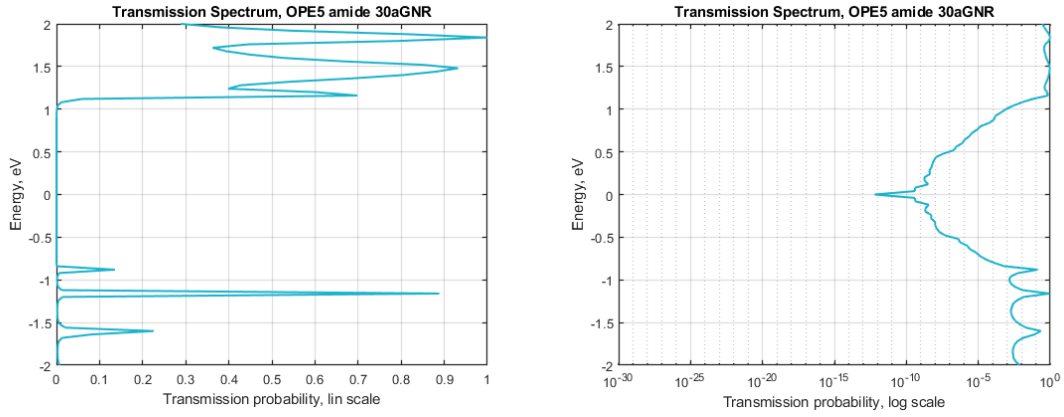


Figure 3.56. OPE5+amide GMG TS, lin scale Figure 3.57. OPE5+amide GMG TS, log scale

The total current when a  $V_{ds} = 4$  V bias is applied will be lower than the  $25 \mu\text{A}$  of amide-free OPE3 SMJ, since experimentally amide decreases the current, giving instead stability and avoiding spurious rotations, figure 3.58.

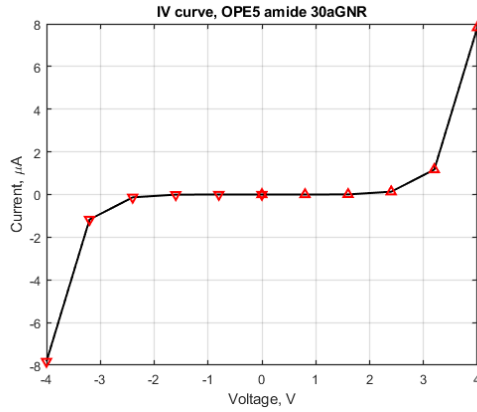


Figure 3.58. OPE5+amide GMG-SMJ I-V characteristic

The electronic path is shown to visualize the open and closed channel for the two states of a possible transistor, figure 3.59 and 3.60.

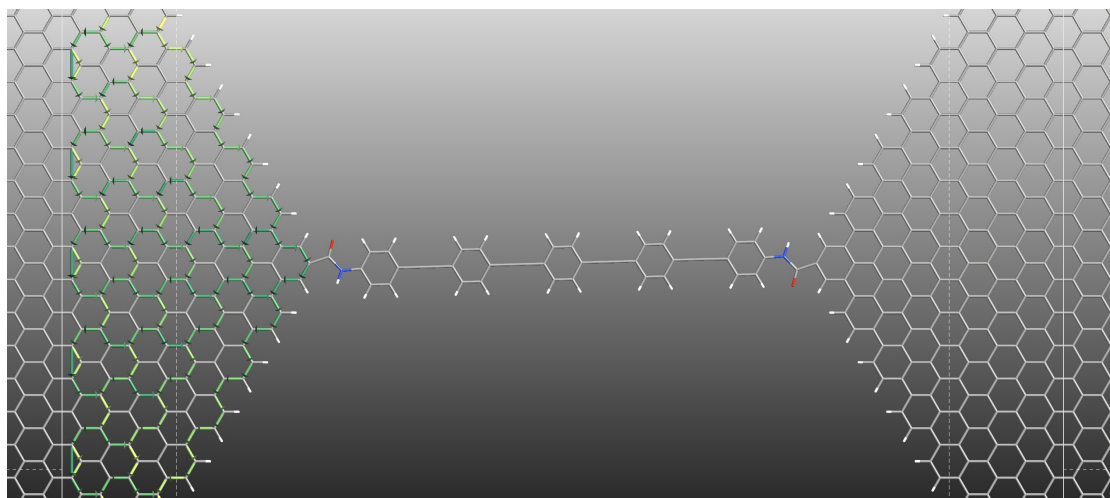


Figure 3.59. OPE5+amide electron pathways, OFF state, 0 eV

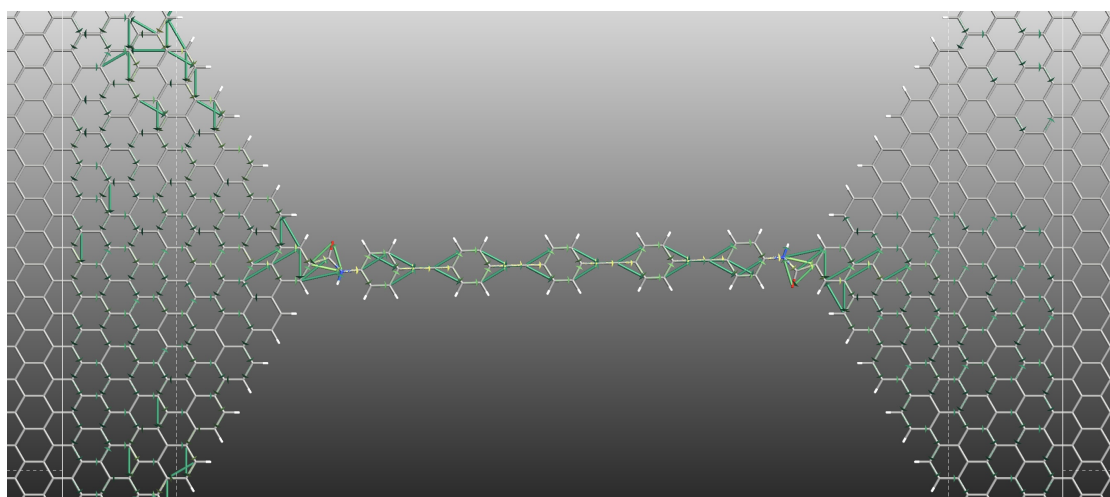


Figure 3.60. OPE5+amide electron pathways, ON state, HOMO-1 =  $-1.16$  eV with  $T=0.89$

### 3.10 pCp with amide linkers and graphene electrodes

The last device is a [3.3]pCp linked by amide groups to large real graphene electrodes.

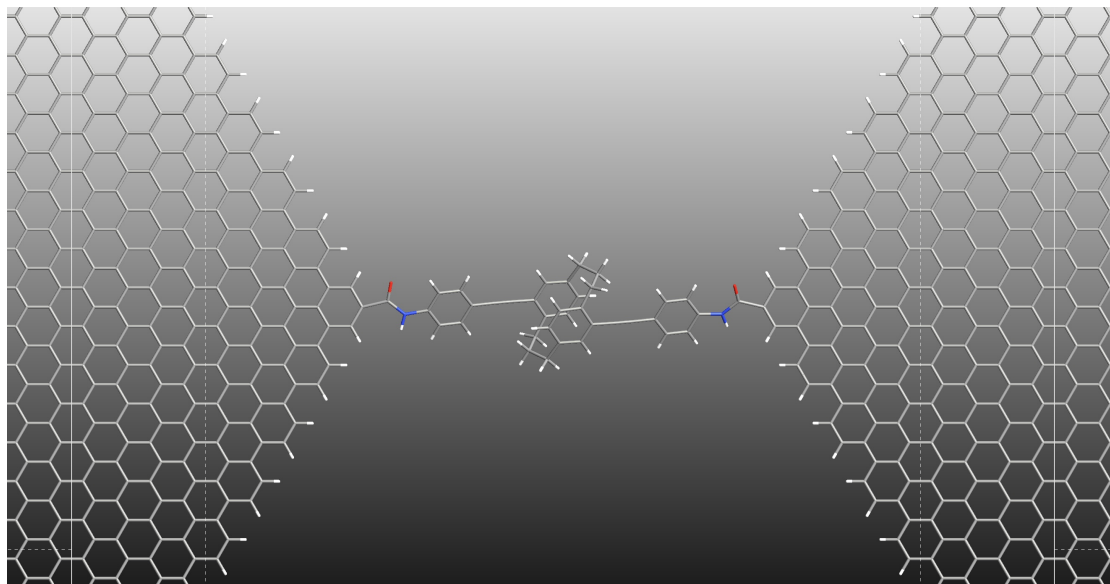


Figure 3.61. [3.3]pCp amide-linked graphene-based single molecule junction

A [3.3] paracyclophane made by two OPE structures is terminated by amide linkages. The simulation is optimized to obtain an accurate 3D geometry<sup>T.5</sup> with right bond lengths. The DOS, figure 3.62, follows the peaks of the molecule with amide that broads LUMOs and quenches HOMOs (as for OPEs, figure 3.63), as confirmed by TS, figure 3.64.

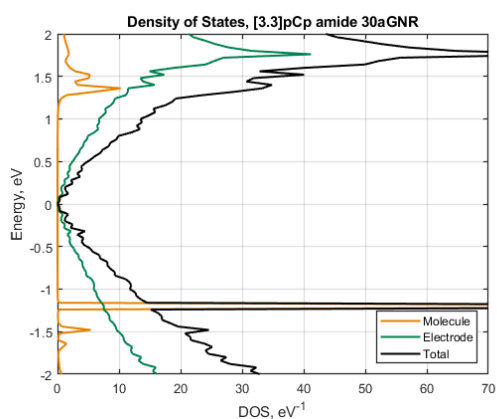


Figure 3.62. pCp+amide GMG DOS

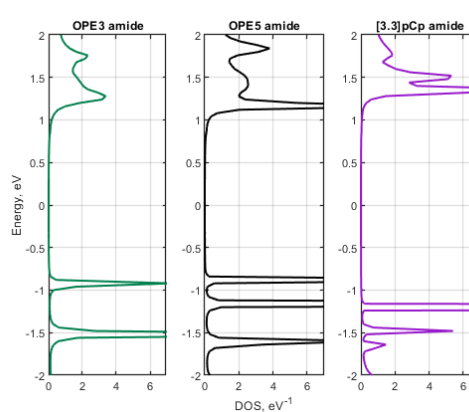


Figure 3.63. Mol+amide DOS comparison

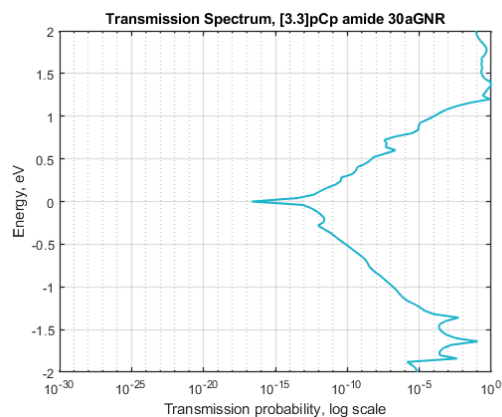
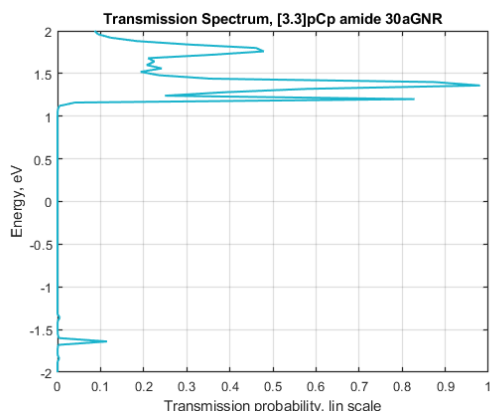


Figure 3.64. pCp+amide GMG TS, lin scale    Figure 3.65. pCp+amide GMG TS, log scale

Depending on how external and facing rings are geometrically connected (with symmetrical or asymmetrical configurations), they can lead to devices that shows constructive (CQI) or destructive quantum interference (DQI) of electron waves passing in the pCp core. This particular *para* configuration exhibits DQI near Fermi energy, giving low conductance state, but CQI otherwise, so with high conductance state<sup>[32]</sup>. The DQI gives a tremendously OFF current, amazing as zero state for a transistor, with transmission of  $T = 10^{-17}$  (figure 3.65), much more than longer amide-linked OPE5 with  $T = 10^{-12}$ . With gold electrodes same pCp SMJ not only requires a backgate to realign the shifted Fermi energy (so DQI OFF state), but such low values cannot be achieved since low electrode states due to the gap are not present. Despite the ON current is not high, figure 3.66, the ON/OFF ratio is excellent, and the junction can be also exploited as a sensor for guesting molecules in the pCp core (e.g. Cr) that gives CQI in the Fermi range (so high conductance state), operating in the ON empty molecule point as OFF of the sensor<sup>[33]</sup>.

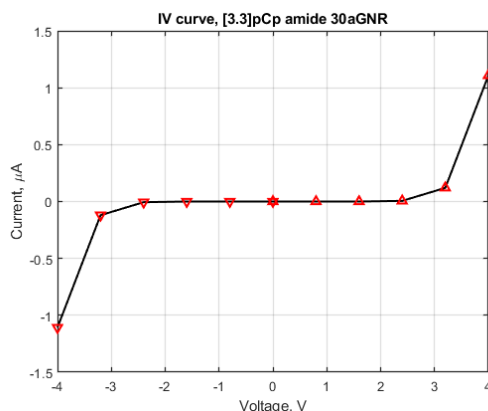


Figure 3.66. pCp+amide GMG-SMJ I-V characteristic



The electronic path is shown for the OFF state 3.67. For the ON state, figure 3.68 shows how the electronegativity of Oxygen helps capturing electrons in the amide contribute; and the resonance in the  $\pi$ -stacked hydrocarbons (flows' intensity from green to yellow).

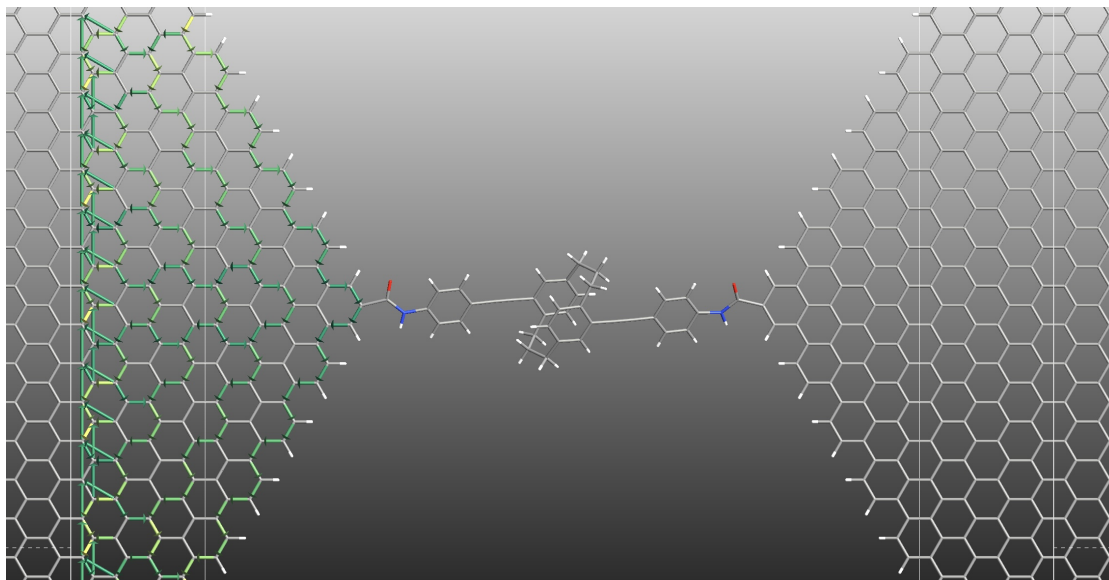


Figure 3.67. pCp+amide electron pathways, OFF state, 0eV

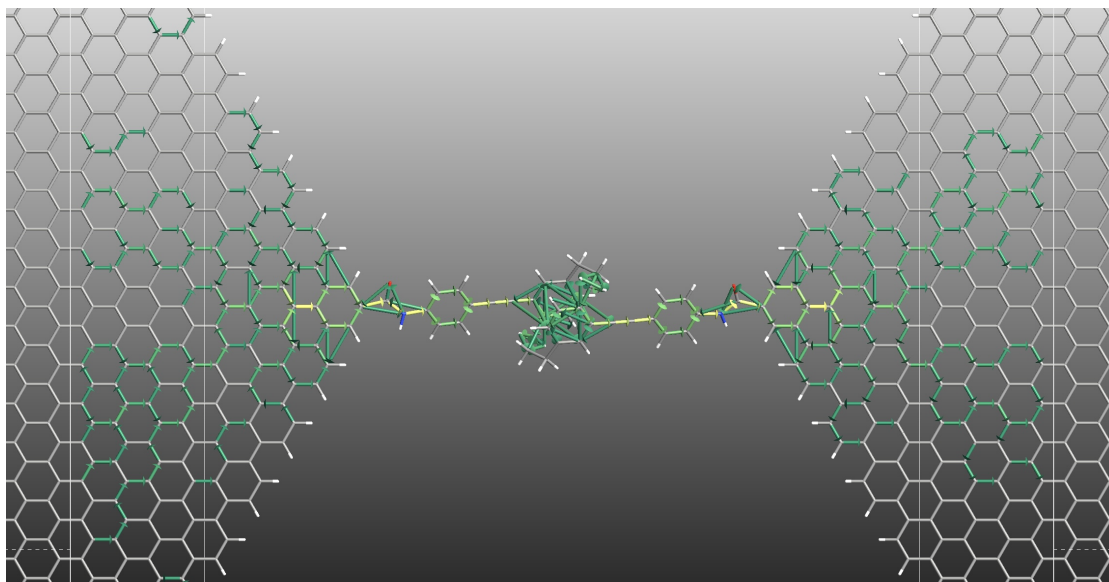


Figure 3.68. pCp+amide electron pathways, ON state, LUMO+1 = 1.36eV with T=0.99



### 3.11 Conclusions and future works

All these simulations have shown how molecules properties play a fundamental role in the final conductance, modulating the peaks in the TS and so ruling the transport mechanisms: they are indeed called *molecular* junctions.

The results of the graphene-based SMJs simulations have shown how larger electrodes give more coupling with the molecules, being also bigger reservoirs of conductive states: the DOS of 30aGNR-based electrodes is tripled compared to 9aGNR ones; also in the OFF current  $T$  was higher with the same molecule barrier width.

The amide group, optimal for stability and  $\pi$ -delocalization, has been shown a tendency to broaden LUMO states while isolating HOMO ones, both for the OPEs and pCp.

Also from the electron pathways it has been seen how oxygen electronegativity and N-C=O resonance favour the transport.

The [3.3]pCp has been shown an extremely high ON/OFF ratio thanks to DQI and graphene gap. Unfortunately it has not been possible to precisely evaluate its order of magnitude because the current has been measured at 0 V bias (giving precisely 0  $\mu$ A OFF) and with the first point at 0.8 V, out of the OFF state. Consider that each current point requires brand new density matrix calculations and its TS evaluation, increasing the simulation time by days. However, since the current is given by integrating TS, the ratio has for all the simulations approximately the same order of magnitude of  $T(\text{OFF})$ .

In general graphene electrodes have been shown not to negatively affect the properties of the molecule, not shifting its Fermi level as happens with gold (needing an additional backgate voltage); lowering instead the H-L gap and obtaining current values much higher than the corresponding ones of gold-SMJs found in literature.

All the simulations have been launched taking into account the fabrication methods of Chapter 2, reproducing realistic devices quite faithfully.

The results have been all consistent with the conduction theory analytically analyzed in Chapter 1.

The next steps to this Thesis could be:

- A more detailed analytical study on graphene and GNR conduction, considering edge states or complicating the Landauer model considering scattering or e-e interaction, temperature dependence etc.
- A more in-depth look at graphene-based break-junctions creation methods, see how gap lengths are estimated, for example with the Simmons model.
- A numerical study of the tunneling current based on the barrier energy of the graphene electrode tips.
- New simulations with different molecules and/or anchoring groups, e.g. 3D  $\pi$ -stacking linkers. A comparison with metal electrodes and a more accurate analysis of electrode DOS and their respective orbitals and transmission eigenstates. Also with better mesh-refined of k-points for more accurate results.
- An analysis with an applied Gate Voltage for shifting molecule levels, studying the transcharacteristic of a possible GMG-SMJ transistor.



# Appendix A

## E(k) derivation

### A.1 Tight binding method

The derivation of the energy band diagram for the graphene sheet starts from the time independent Schrödinger equation of the whole lattice:

$$\hat{\mathcal{H}}\psi_{\mathbf{k}}(\mathbf{r}) = E_{\mathbf{k}}\psi_{\mathbf{k}}(\mathbf{r}) \quad (\text{A.1})$$

In order to solve it mathematically it is convenient to make the so called projection of Schrödinger equation on the atomic wavefunction  $\Phi_{0A}^{at}$  (and simultaneously with  $\Phi_{0B}^{at}$ ): both members are multiplied by the complex conjugated wavefunction of the atoms at the origin, and then integrated over the whole space.

$$\begin{cases} \int \Phi_{0A}^*(\mathbf{r})\hat{\mathcal{H}}\psi_{\mathbf{k}}(\mathbf{r})d\mathbf{r} = E_{\mathbf{k}} \int \Phi_{0A}^*(\mathbf{r})\psi_{\mathbf{k}}(\mathbf{r})d\mathbf{r} & \Phi_{0A}(\mathbf{r}) = \Phi_{2pz}^{at}(\mathbf{r} - \boldsymbol{\delta}_3) \\ \int \Phi_{0B}^*(\mathbf{r})\hat{\mathcal{H}}\psi_{\mathbf{k}}(\mathbf{r})d\mathbf{r} = E_{\mathbf{k}} \int \Phi_{0B}^*(\mathbf{r})\psi_{\mathbf{k}}(\mathbf{r})d\mathbf{r} & \Phi_{0B}(\mathbf{r}) = \Phi_{2pz}^{at}(\mathbf{r}) \end{cases} \quad (\text{A.2})$$

Having as shown in equation (1.9)

$$\psi_{\mathbf{k}}(\mathbf{r}) = f_{\mathbf{k}A}\psi_{\mathbf{k}A}(\mathbf{r}) + f_{\mathbf{k}B}\psi_{\mathbf{k}B}(\mathbf{r}) \quad (\text{A.3})$$

it is possible to write equation (A.2) in a compact form,

$$\begin{cases} f_{\mathbf{k}A}H_{AA} + f_{\mathbf{k}B}H_{AB} = E_{\mathbf{k}}(f_{\mathbf{k}A}S_{AA} + f_{\mathbf{k}B}S_{AB}) \\ f_{\mathbf{k}A}H_{BA} + f_{\mathbf{k}B}H_{BB} = E_{\mathbf{k}}(f_{\mathbf{k}A}S_{BA} + f_{\mathbf{k}B}S_{BB}) \end{cases} \quad (\text{A.4})$$

defining the Hamiltonian and Superposition integrals as:

$$H_{\alpha\beta} = \int \Phi_{0\alpha}^*(\mathbf{r})\hat{\mathcal{H}}\psi_{\mathbf{k}\beta}(\mathbf{r})d\mathbf{r} \quad \alpha, \beta = A, B \quad (\text{A.5})$$

$$S_{\alpha\beta} = \int \Phi_{0\alpha}^*(\mathbf{r})\psi_{\mathbf{k}\beta}(\mathbf{r})d\mathbf{r} \quad \alpha, \beta = A, B \quad (\text{A.6})$$

Now since the lattice Hamiltonian reads as

$$\hat{\mathcal{H}} = -\frac{\hbar^2 \nabla^2}{2m} + U^{lat}(\mathbf{r}) \quad (\text{A.7})$$

it is necessary to rewrite  $\hat{\mathcal{H}}$  from  $\hat{\mathcal{H}}^{lat}$  to  $\hat{\mathcal{H}}^{at}$ :

$$\begin{aligned} H_{\alpha\beta} &= \int \Phi_{0\alpha}^*(\mathbf{r}) \left( \hat{\mathcal{H}} + U_{0\alpha}^{at}(\mathbf{r}) - U_{0\alpha}^{lat}(\mathbf{r}) \right) \psi_{\mathbf{k}\beta}(\mathbf{r}) d\mathbf{r} \\ &= \int \Phi_{0\alpha}^*(\mathbf{r}) \left( \hat{\mathcal{H}}_{0\alpha}^{at} + U^{lat}(\mathbf{r}) - U_{0\alpha}^{at}(\mathbf{r}) \right) \psi_{\mathbf{k}\beta}(\mathbf{r}) d\mathbf{r} \\ &= \int \Phi_{0\alpha}^*(\mathbf{r}) \hat{\mathcal{H}}_{0\alpha}^{at} \psi_{\mathbf{k}\beta}(\mathbf{r}) d\mathbf{r} + \underbrace{\int \Phi_{0\alpha}^*(\mathbf{r}) \left( U^{lat}(\mathbf{r}) - U_{0\alpha}^{at}(\mathbf{r}) \right) \psi_{\mathbf{k}\beta}(\mathbf{r}) d\mathbf{r}}_{\Delta U_{\alpha}(\mathbf{r})} \end{aligned} \quad (\text{A.8})$$

where  $\Delta U_{\alpha}(\mathbf{r})$  is the potential difference of the total lattice potential  $U^{lat}(\mathbf{r})$  given by all the atoms, and the potential  $U_{0\alpha}^{at}(\mathbf{r})$  given by the  $\alpha$  atoms of the  $\mathbf{R} = 0$  site.

$$V_{\alpha\beta} = \int \Phi_{0\alpha}^*(\mathbf{r}) \Delta U_{\alpha}(\mathbf{r}) \psi_{\mathbf{k}\beta}(\mathbf{r}) d\mathbf{r} \quad (\text{A.9})$$

Using the upper (A.9) equation, and exploiting the  $\hat{\mathcal{H}}$  Hermitian properties,  $H_{\alpha\beta}$  can be finally simplified in the compact form:

$$\begin{aligned} H_{\alpha\beta} &= \int \Phi_{0\alpha}^*(\mathbf{r}) \hat{\mathcal{H}}_{0\alpha}^{at} \psi_{\mathbf{k}\beta}(\mathbf{r}) d\mathbf{r} + V_{\alpha\beta} \\ &= \left( \int \psi_{\mathbf{k}\beta}(\mathbf{r})^* \underbrace{\hat{\mathcal{H}}_{0\alpha}^{at} \Phi_{0\alpha}(\mathbf{r}) d\mathbf{r}}_{=E^{at}\Phi_{0\alpha}(\mathbf{r})} \right)^* + V_{\alpha\beta} \\ &= E^{at} \int \Phi_{0\alpha}^*(\mathbf{r}) \psi_{\mathbf{k}\beta}(\mathbf{r}) d\mathbf{r} + V_{\alpha\beta} \\ &= E^{at} S_{\alpha\beta} + V_{\alpha\beta} \end{aligned} \quad (\text{A.10})$$

So  $H_{\alpha\beta}$  can be substituted into (A.4), leading to the linear equation system:

$$\begin{cases} (V_{AA} - (E_{\mathbf{k}} - E^{at})S_{AA})f_{\mathbf{k}A} + (V_{AB} - (E_{\mathbf{k}} - E^{at})S_{AB})f_{\mathbf{k}B} = 0 \\ (V_{BA} - (E_{\mathbf{k}} - E^{at})S_{BA})f_{\mathbf{k}A} + (V_{BB} - (E_{\mathbf{k}} - E^{at})S_{BB})f_{\mathbf{k}B} = 0 \end{cases} \quad (\text{A.11})$$

that can be represent in the matrix form:

$$\begin{pmatrix} V_{AA} - \varepsilon_{\mathbf{k}}S_{AA} & V_{AB} - \varepsilon_{\mathbf{k}}S_{AB} \\ V_{BA} - \varepsilon_{\mathbf{k}}S_{BA} & V_{BB} - \varepsilon_{\mathbf{k}}S_{BB} \end{pmatrix} \begin{pmatrix} f_{\mathbf{k}A} \\ f_{\mathbf{k}B} \end{pmatrix} = \begin{pmatrix} 0 \\ 0 \end{pmatrix} \quad (\text{A.12})$$

$$\varepsilon_{\mathbf{k}} = E_{\mathbf{k}} - E^{at} \quad (\text{A.13})$$

where the new energy  $\varepsilon_{\mathbf{k}}$  represents the actual  $E_{\mathbf{k}}$  energy level of the graphene sheet minus an arbitrary constant, set equal to the atomic Carbon energy  $E^{at}$  of the non-bonded atoms.

### A.1.1 Nearest-Neighbours approximation

As seen in equation (1.10), the wavefunctions are imposed by the Bloch theorem in the form:

$$\begin{cases} \psi_{\mathbf{k}A}(\mathbf{r}) = \frac{1}{\sqrt{N}} \sum_{\mathbf{R}} e^{i\mathbf{k}\cdot\mathbf{R}} \Phi_{2pz}^{at}(\mathbf{r} - \mathbf{R}_A) & \mathbf{R}_A = \mathbf{R} + \delta_3 \\ \psi_{\mathbf{k}B}(\mathbf{r}) = \frac{1}{\sqrt{N}} \sum_{\mathbf{R}} e^{i\mathbf{k}\cdot\mathbf{R}} \Phi_{2pz}^{at}(\mathbf{r} - \mathbf{R}_B) & \mathbf{R}_B = \mathbf{R} \end{cases} \quad (\text{A.14})$$

so to find analytically the energy  $\varepsilon(\mathbf{k})$  of equation (A.12), it is necessary to simplify the  $V_{\alpha\beta}$  and  $S_{\alpha\beta}$  of (A.9) and (A.6) respectively, limiting the wavefunctions interactions to only their nearest neighbours. This approximation can be considered quite fair since the carbon sites decrease their interaction as they move away from each others, so both overlap integral and potential tend to zero for distant atoms. In particular, in this n-n approximation, a B site will have 3 A neighbours sites, and viceversa, as shown in the 1.3 lattice.

For example in the  $V_{BB}$  integral, since it considers only B-sites nearest to the  $\Phi_{0B}(\mathbf{r})$  site, it takes into account only the 0B site itself (the one with  $\mathbf{R} = 0$ ). So the superposition of the total wavefunctions becomes  $\psi_{\mathbf{k}B}(\mathbf{r}) \rightarrow \Phi_{0B}(\mathbf{r}) = \Phi_{2pz}^{at}(\mathbf{r})$ :

$$\begin{aligned} V_{BB} &= \int \Phi_{0B}^*(\mathbf{r}) \Delta U_B(\mathbf{r}) \psi_{\mathbf{k}B}(\mathbf{r}) d\mathbf{r} \\ &= \int \Phi_{2pz}^{at*}(\mathbf{r}) \left( U^{lat}(\mathbf{r}) - U_{0B}^{at}(\mathbf{r}) \right) \left( \frac{1}{\sqrt{N}} \sum_{\mathbf{R}} e^{i\mathbf{k}\cdot\mathbf{R}} \Phi_{2pz}^{at}(\mathbf{r} - \mathbf{R}_B) \right) d\mathbf{r} \\ &\simeq \int \Phi_{2pz}^{at*}(\mathbf{r}) \Delta U_B(\mathbf{r}) \frac{1}{\sqrt{N}} \Phi_{2pz}^{at}(\mathbf{r}) d\mathbf{r} \\ &\simeq \frac{1}{\sqrt{N}} \sigma \end{aligned} \quad (\text{A.15})$$

With the same approximation one can obtain all  $V_{\alpha\beta}$  and correspondingly  $S_{\alpha\beta}$  (just  $V_{\alpha\beta}$  when  $\Delta U \rightarrow 1$ ), reported except the  $\sqrt{N}$  constant factor simplifiable in all terms on eq (A.12):

$$\begin{cases} V_{AA} = \sigma \\ V_{BB} = \sigma \\ V_{AB} = \alpha^*(\mathbf{k})\gamma^* \\ V_{BA} = \alpha(\mathbf{k})\gamma \\ S_{AA} = 1 \\ S_{BB} = 1 \\ S_{AB} = \alpha^*(\mathbf{k})s^* \\ S_{BA} = \alpha(\mathbf{k})s \end{cases} \quad (\text{A.16})$$

$$\left\{ \begin{array}{l} \sigma \doteq \int \Phi_{2pz}^{at*}(\mathbf{r}) \Delta U_B(\mathbf{r}) \Phi_{2pz}^{at}(\mathbf{r}) d\mathbf{r} \\ \gamma \doteq \int \Phi_{2pz}^{at*}(\mathbf{r}) \Delta U_B(\mathbf{r}) \Phi_{2pz}^{at}(\mathbf{r} - \boldsymbol{\delta}_3) d\mathbf{r} \\ s \doteq \int \Phi_{2pz}^{at*}(\mathbf{r}) \Phi_{2pz}^{at}(\mathbf{r} - \boldsymbol{\delta}_3) d\mathbf{r} \\ \alpha(\mathbf{k}) \doteq \sum_{i=1}^3 e^{i\mathbf{k} \cdot (\boldsymbol{\delta}_i - \boldsymbol{\delta}_3)} = 1 + e^{i\mathbf{k} \cdot \mathbf{a}_1} + e^{i\mathbf{k} \cdot \mathbf{a}_2} \end{array} \right. \quad (\text{A.17})$$

Now the last assumption is to set the atomic site potential equal to the carbon atom potential  $U_0(\mathbf{r}) \simeq U^{at}(\mathbf{r})$ , explained in equation (1.8), obtaining for  $\Delta U(\mathbf{r})$ :

$$\begin{aligned} \Delta U_B(\mathbf{r}) &= U^{lat}(\mathbf{r}) - U_{0B}^{at}(\mathbf{r}) \\ &= \sum_{\mathbf{R}} \left( U_0(\mathbf{r} - \mathbf{R}) + U_0(\mathbf{r} - \mathbf{R} - \boldsymbol{\delta}_3) \right) - U^{at}(\mathbf{r}) \\ &\simeq \sum_{\mathbf{R}} \left( U^{at}(\mathbf{r} - \mathbf{R}) + U^{at}(\mathbf{r} - \mathbf{R} - \boldsymbol{\delta}_3) \right) - U^{at}(\mathbf{r}) \\ &\simeq U^{at}(\mathbf{r} - \boldsymbol{\delta}_3) + \sum_{\mathbf{R} \neq \mathbf{0}} \left( U^{at}(\mathbf{r} - \mathbf{R}) + U^{at}(\mathbf{r} - \mathbf{R} - \boldsymbol{\delta}_3) \right) \end{aligned} \quad (\text{A.18})$$

and so rewriting the  $\sigma$ ,  $\gamma$ ,  $s$  therms with the atomic potential assumption and the n-n approximation, the  $\sigma_0$  integral considers the contribution of the 3 nearest A-sites (so multiplied by a factor 3), while in the  $\gamma_0$  integral remains only the atomic potential translated on the A site ( $U^{at}(\mathbf{r} - \boldsymbol{\delta}_3)$ ):

$$\left\{ \begin{array}{l} \sigma_0 \doteq 3 \int \Phi_{2pz}^{at*}(\mathbf{r}) U^{at}(\mathbf{r} - \boldsymbol{\delta}_3) \Phi_{2pz}^{at}(\mathbf{r}) d\mathbf{r} \\ \gamma_0 \doteq \int \Phi_{2pz}^{at*}(\mathbf{r}) U^{at}(\mathbf{r} - \boldsymbol{\delta}_3) \Phi_{2pz}^{at}(\mathbf{r} - \boldsymbol{\delta}_3) d\mathbf{r} \\ s_0 \doteq \int \Phi_{2pz}^{at*}(\mathbf{r}) \Phi_{2pz}^{at}(\mathbf{r} - \boldsymbol{\delta}_3) d\mathbf{r} \end{array} \right. \quad (\text{A.19})$$

where these integrals depend only by the  $U^{at}$  and  $\Phi_{spz}^{at}$  of carbon atoms, found in the literature. Finally (A.12) becomes:

$$\begin{pmatrix} -\sigma_0 - \varepsilon_{\mathbf{k}} & -\alpha^*(\mathbf{k})(\gamma_0 + \varepsilon_{\mathbf{k}} s_0) \\ -\alpha(\mathbf{k})(\gamma_0 + \varepsilon_{\mathbf{k}} s_0) & -\sigma_0 - \varepsilon_{\mathbf{k}} \end{pmatrix} \begin{pmatrix} f_{\mathbf{k}A} \\ f_{\mathbf{k}B} \end{pmatrix} = \begin{pmatrix} 0 \\ 0 \end{pmatrix} \quad (\text{A.20})$$

where the determinant is equal to zero if

$$(\sigma_0 + \varepsilon_{\mathbf{k}})^2 = |\alpha(\mathbf{k})|^2 (\gamma_0 + \varepsilon_{\mathbf{k}} s_0)^2 \quad (\text{A.21})$$

giving two solutions

$$\varepsilon_{\mathbf{k}}^{\pm} = \frac{-\sigma_0 \pm \gamma_0 |\alpha(\mathbf{k})|}{1 \mp s_0 |\alpha(\mathbf{k})|} \quad (\text{A.22})$$

It is important to mention that these values of the energy do not depend from the coefficients  $f_{\mathbf{k}A}$  and  $f_{\mathbf{k}B}$  of the A and B sites of the total wavefunction  $\psi_{\mathbf{k}}(\mathbf{r})$ . The localization of the wavefunction and so the spatial position of the orbitals (the electron cloud) are governed by spin rules.





# Simulations parameters

Here are reported all the parameters set for the different simulations launched in the Thesis. For the 2D devices of Chapter 3 it has been used the setup explained in Section 3.1, except for 3D pCp structure that also requires k-sampling in the third dimension. Other parameters are set by default to 2022.03 version.

All graphs are elaborated with the MathWorks Inc. MATLAB® Software 2022b version.

Table T.1. Graphene sheet (primitive cell) Band Structure parameters

Calculator	Pseudopotential	Basis set	k-points sampling
LCAO	FHI	DZDP	$n_a = 1, n_b = 9, n_c = 9$
BS sampling		BS path	
n=10001		[G,Z]	

Table T.2. Graphene sheet (primitive cell) Density of States parameters

Calculator	Pseudopotential	Basis set	k-points sampling
LCAO	FHI	DZDP	$n_a = 1, n_b = 9, n_c = 9$
DOS bands		DOS k-points	
50		$n_b = n_c = 333$	

Table T.3. Graphene sheet (primitive cell) Transmission Spectrum parameters

Calculator	Pseudopotential	Basis set	k-points sampling
LCAO	FHI	DZDP	$n_a = 1, n_b = 9, n_c = 9$
TS range		TS k-points	
[-2,2]eV		$n_b = n_c = 333$	

Table T.4. 9aGNR and 30aGNR BS, DOS and TS parameters

Calculator	Pseudopotential	Basis set	k-points sampling
LCAO	FHI	DZDP	$n_a = 1, n_b = 9, n_c = 9$
BS sampling	BS path	DOS k-points	TS k-points
n=1001	[G,Z]	$n_a = 1, n_b = 123$	$n_a = 1, n_b = 123$

Table T.5. [3.3]pCp+amide with large graphene electrodes device parameters

Calculator	Pseudopotential	Basis set	k-points sampling
LCAO	FHI	DZDP	$n_a = 3, n_b = 9, n_c = 27$
DOS k-points	TS k-points	IV k-points	Pathways k-points
$n_a = 3, n_b = 9$	$n_a = 3, n_b = 9$	$n_a = 3, n_b = 9$	$n_a = 3, n_b = 9$



# Bibliography

- [1] KATSNELSON, Mikhail I. Graphene: carbon in two dimensions. Materials today, 2007.
- [2] REICH, Stephanie, et al. Tight-binding description of graphene. Physical Review B, 2002, 66.3: 035412.
- [3] SARMA, S. Das, et al. Electronic transport in two-dimensional graphene. Reviews of modern physics, 2011, 83.2: 407.
- [4] NETO, AH Castro, et al. The electronic properties of graphene. Reviews of modern physics, 2009, 81.1: 109.
- [5] DATTA, Supriyo. Quantum transport: atom to transistor. Cambridge university press, 2005.
- [6] BERDEBES, Dionisis, et al. Low bias transport in graphene: An introduction. NCN@ Purdue Summer School: Electronics from the Bottom Up, 2009.
- [7] CASTRO, Eduardo V., et al. Biased bilayer graphene: semiconductor with a gap tunable by the electric field effect. Physical review letters, 2007, 99.21: 216802.
- [8] BREY, Luis; SENEOR, Pierre; TEJEDA, Antonio. Graphene Nanoribbons. 2019.
- [9] ONIPKO, Alexander. Spectrum of  $\pi$  electrons in graphene as an alternant macro-molecule and its specific features in quantum conductance. Physical Review B, 2008, 78.24: 245412.
- [10] WAKABAYASHI, Katsunori, et al. Electronic states of graphene nanoribbons and analytical solutions. Science and technology of advanced materials, 2010, 11.5: 054504.
- [11] ZHENG, Huaixiu, et al. Analytical study of electronic structure in armchair graphene nanoribbons. Physical Review B, 2007, 75.16: 165414.
- [12] SON, Young-Woo; COHEN, Marvin L.; LOUIE, Steven G. Energy gaps in graphene nanoribbons. Physical review letters, 2006, 97.21: 216803.
- [13] NAKADA, Kyoko, et al. Edge state in graphene ribbons: Nanometer size effect and edge shape dependence. Physical Review B, 1996, 54.24: 17954.

- [14] XU, Hengyi; HEINZEL, T.; ZOZOULENKO, I. V. Edge disorder and localization regimes in bilayer graphene nanoribbons. *Physical Review B*, 2009, 80.4: 045308.
- [15] PERES, N. M. R.; NETO, AH Castro; GUINEA, F. Conductance quantization in mesoscopic graphene. *Physical Review B*, 2006, 73.19: 195411.
- [16] LIN, Yu-Ming, et al. Electrical observation of subband formation in graphene nanoribbons. *Physical Review B*, 2008, 78.16: 161409.
- [17] YEH, Nai-Chang, et al. Single-step growth of graphene and graphene-based nanostructures by plasma-enhanced chemical vapor deposition. *Nanotechnology*, 2019, 30.16: 162001.
- [18] WARNER, Jamie H., et al. Chapter 6-Applications of Graphene. *Graphene*; Elsevier: Amsterdam, The Netherlands, 2013, 333-437.
- [19] WANG, Xinran; DAI, Hongjie. Etching and narrowing of graphene from the edges. *Nature chemistry*, 2010, 2.8: 661-665.
- [20] YANG, Caiyao, et al. Fabrication and functions of graphene–molecule–graphene single-molecule junctions. *The Journal of Chemical Physics*, 2020, 152.12: 120902.
- [21] MENG, Linan, et al. Dual-gated single-molecule field-effect transistors beyond Moore’s law. *Nature communications*, 2022, 13.1: 1410.
- [22] XIE, Xinmiao, et al. Single-molecule junction: A reliable platform for monitoring molecular physical and chemical processes. *ACS nano*, 2022, 16.3: 3476-3505.
- [23] GEHRING, Pascal; THIJSEN, Jos M.; VAN DER ZANT, Herre SJ. Single-molecule quantum-transport phenomena in break junctions. *Nature Reviews Physics*, 2019, 1.6: 381-396.
- [24] ZHAO, Shiqiang, et al. Non-covalent interaction-based molecular electronics with graphene electrodes. *Nano Research*, 2021, 1-11.
- [25] TAO, Shuhui, et al. Graphene-contacted single molecular junctions with conjugated molecular wires. *ACS Applied Nano Materials*, 2018, 2.1: 12-18.
- [26] JIA, Chuancheng, et al. Carbon electrode–molecule junctions: A reliable platform for molecular electronics. *Accounts of chemical research*, 2015, 48.9: 2565-2575.
- [27] FU, Huanyan, et al. Dipole-improved gating of azulene-based single-molecule transistors. *Journal of Materials Chemistry C*, 2022, 10.20: 7803-7809.
- [28] PRINS, Ferry, et al. Room-temperature gating of molecular junctions using few-layer graphene nanogap electrodes. *Nano letters*, 2011, 11.11: 4607-4611.
- [29] SIMMONS, John G. Generalized formula for the electric tunnel effect between similar electrodes separated by a thin insulating film. *Journal of applied physics*, 1963, 34.6: 1793-1803.

## BIBLIOGRAPHY

---

- [30] EL ABBASSI, Maria, et al. From electroburning to sublimation: substrate and environmental effects in the electrical breakdown process of monolayer graphene. *Nanoscale*, 2017, 9.44: 17312-17317.
  - [31] CAO, Yang, et al. Building high-throughput molecular junctions using indented graphene point contacts. *Angewandte Chemie*, 2012, 124.49: 12394-12398.
  - [32] DAS, Bidisa; ABE, Shuji. Designing cyclophane-based molecular wire sensors. *The Journal of Physical Chemistry B*, 2006, 110.47: 23806-23811.
  - [33] REZNIKOVA, Ksenia, et al. Substitution Pattern Controlled Quantum Interference in [2.2] Paracyclophane-Based Single-Molecule Junctions. *Journal of the American Chemical Society*, 2021, 143.34: 13944-13951.
- [M] MANUAL: Synopsys' QuantumATK® T-2022.03 Documentation.